



HAL
open science

A simple method for earthquake location by surface-wave time reversal

Lapo Boschi, Irene Molinari, Michael Reinwald

► **To cite this version:**

Lapo Boschi, Irene Molinari, Michael Reinwald. A simple method for earthquake location by surface-wave time reversal. *Geophysical Journal International*, 2018, 215 (1), pp.1-21. 10.1093/gji/ggy261 . hal-01930079

HAL Id: hal-01930079

<https://hal.sorbonne-universite.fr/hal-01930079>

Submitted on 21 Nov 2018

HAL is a multi-disciplinary open access archive for the deposit and dissemination of scientific research documents, whether they are published or not. The documents may come from teaching and research institutions in France or abroad, or from public or private research centers.

L'archive ouverte pluridisciplinaire **HAL**, est destinée au dépôt et à la diffusion de documents scientifiques de niveau recherche, publiés ou non, émanant des établissements d'enseignement et de recherche français ou étrangers, des laboratoires publics ou privés.

A simple method for earthquake location by surface-wave time-reversal

Lapo Boschi¹, Irene Molinari², and Michael Reinwald³

¹Sorbonne Université, CNRS-INSU, Institut des Sciences de la Terre Paris, ISTE-P
UMR 7193, F-75005 Paris, France

²Institute of Geophysics, ETH Zurich, Sonneggstr. 5, CH-8092 Zürich, Switzerland

³Sorbonne Université, CNRS, INSERM, Laboratoire d'Imagerie Biomédicale, LIB,
F-75006 Paris, France

June 26, 2018

Abstract

The scalar 2-D Helmholtz' equation (i.e., “membrane waves”) can be used to model surface-wave propagation in a laterally smooth, lossless half space. Building on this known result, we develop an algorithm to localize earthquake sources based on surface-wave data, via numerical time-reversal on a membrane, where monochromatic waves propagate with the phase velocity of Rayleigh or Love waves at the same frequency. By conducting monochromatic membrane-wave time-reversal simulations at various frequencies and combining the results, broadband time-reversed surface waves can be modeled. Importantly, membrane-wave modeling is computationally much less expensive than three-dimensional surface-wave modeling. We first explain rigorously the relationship between surface waves and membrane waves. Our mathematical treatment is slightly different from those found in the literature, in that it does not invoke variational principles. We next implement our time-reversal algorithm via spectral elements as well as simple ray tracing. Both implementations account for the effects of lateral variations in phase velocity. We validate the two resulting tools by means of several numerical experiments. This includes synthetic tests, as well as the localization of a virtual source based on a data set of real ambient-noise cross correlations, and the localization of the epicenter of a real earthquake from real, raw data. In this study, applications are limited to Northern Italy and the Alpine arc, where we have access to recent, high resolution phase velocity maps, ambient-noise cross correlations and data from a recent, relatively large earthquake. The accuracy of epicenter location despite non-uniformity in station coverage encourages further applications of our method, in particular to the task of mapping large-earthquake rupture in space and time.

1 Introduction

Estimates of seismic slip as a function of position and time for a given earthquake are obtained today in different ways, depending on the magnitude and depth of the earthquake, and

35 on the instrumental coverage. Several different types of seismic and geodetic observations are
36 employed. Dense networks of strong-motion accelerometers are currently deployed in seismic
37 regions worldwide; they are designed to record the high-frequency oscillations generated by
38 a nearby event, but they have little sensitivity to the lower frequencies, and cannot be used
39 to constrain the properties of far earthquakes. At the opposite end of the frequency spec-
40 trum, data from GPS networks and satellite geodesy are used as constraints of the final slip
41 associated with an earthquake; they provide good resolution of the surface expression of the
42 rupture, but have little or no sensitivity to fault geometry at depth [e.g. *Mai et al.*, 2016, and
43 references therein]. Wherever the coverage provided by nearby instruments is insufficient,
44 local and/or global broadband seismic networks at teleseismic distances are used to image
45 slip. As a general rule, fault geometry is particularly hard to constrain on the basis of seismic
46 data alone, and is determined based on geodetic data or, wherever possible, field geology
47 observations.

48 Once a data set for a given event has been compiled, seismic oscillations and geodetic
49 offsets are translated to slip on the fault via (1) least-squares inversions, (2) seismic time
50 reversal, or (3) the back-projection method.

51 (1) Least-squares inversions are based on the representation theorem [e.g. *Aki and Richards*,
52 2002], i.e. the mathematical expression of the physical law relating the geometry of an ar-
53 bitrary rupture to the resulting deformation at any point of a given medium. Because the
54 spatiotemporal evolution of seismic ruptures is generally very complex, it is not surprising
55 that their solutions tend to be very non-unique, as shown in detail by *Mai et al.* [2016].

56 (2) The physics of acoustic or seismic time reversal can be heuristically summarized as
57 follows: a signal is emitted by a source and recorded by multiple receivers; if receivers are
58 then turned into sources, each emitting its own recorded signal (with the corresponding de-
59 lay) flipped with respect to time, the resulting wave field will “focus” at the original source
60 location [e.g. *Fink*, 1999]. This means that by recording real data from an unknown source
61 and then conducting the time-reversal exercise numerically, the location of the source could
62 be determined, provided, of course, that the error associated with modeling of propagation
63 is small, that is to say, that the complexity of the medium of propagation is accounted for
64 within a good approximation. From the standpoint of seismology, this amounts to a kine-
65 matic, extended-source inversion, with the additional possibility of monitoring the backward
66 propagation of time-reversed waves before focusing at the source. In seismology, applications
67 of time reversal [e.g. *Larmat et al.*, 2006, 2008] are hindered by the high computational costs
68 of accurate wave-propagation modeling, unless only very long periods are considered.

69 (3) The back-projection method as described, e.g., by *Ishii et al.* [2005] and currently
70 employed by many authors in seismology, is usually thought of as a simplification of wavefield
71 reverse-time migration, a tool for imaging structure in reflection seismology. This is in many
72 ways similar to time reversal, but involves some further, fundamental simplifications. Namely,
73 the term back-projection refers to studies where the effects of time-reversed wave propagation
74 are not modeled, but approximately corrected for by stacking the signals recorded by an array
75 of nearby receivers. One of the practical consequences of this is that the physical nature of
76 the computed, time-reversed wave field that focuses at the source remains undefined. Its
77 interpretation in terms of rupture mechanics is complicated by the fact, e.g., that it is not
78 known whether it more closely approximates a slip or a rate of slip [*Fukahata et al.*, 2014].

79 We provide in this study the building blocks of a new algorithm for constraining extended-
80 source geometry and time evolution. The algorithm is based on the time-reversal concept, and
81 thus overcomes the limitations of P -wave back-projection, but it is designed so as to reduce
82 significantly the computational costs of full-waveform time reversal. One of the key aspects
83 of our method is that surface waves, instead of P waves, are time-reversed and backward-
84 propagated. This is preferable for several reasons: (i) Surface waves are dispersive, i.e. they
85 “spread out” along the time axis as they travel across the surface of the earth: time reversal
86 turns this process around, enhancing the focusing of backward-propagating waves onto the
87 source. (ii) The problem of surface-wave propagation modeling, although inherently three-
88 dimensional, can be reduced to two dimensions by separating the signal into narrow frequency
89 bands [e.g. *Tanimoto*, 1990; *Tromp and Dahlen*, 1993; *Peter et al.*, 2007, 2009], to be back-
90 projected separately, and subsequently “stacked” together: this reduces the computational
91 costs drastically. (iii) Our knowledge of the three-dimensional structure of the Earth’s deep
92 interior, essential to backward-propagate numerically the time-reversed signal, is limited; but
93 surface-wave propagation is confined to the upper mantle, which is relatively well known;
94 recent, robust global phase-velocity maps of Rayleigh- and Love-wave velocities are available
95 in the frequency band relevant to this project, at the global and, where possible, regional
96 scales [e.g. *Ekström*, 2011; *Kaestle et al.*, 2017]. In seismology/acoustics jargon, point (iii)
97 is equivalent to saying that very accurate surface-wave “Green’s functions” are available and
98 will be used to backward-propagate time-reversed surface-wave data. This further enhances
99 focusing of the time-reversed wave field, and thus the robustness and resolution of mapped
100 seismic slip.

101 We expect our method to be effective over a broad range of epicentral distances. At
102 distances of 30° or more from the epicenter, surface waves carry more energy than body
103 waves, and they can be easily identified and isolated on seismograms. At shorter epicentral
104 distances, where they are obscured by the body-wave coda, surface waves can still emerge in
105 a time-reversal exercise as a result of focusing: this is confirmed by our results, discussed in
106 sec. 6.3.

107 Today, broadband “full-waveform” information is not routinely utilized by researchers
108 interested in mapping the seismic source. Tentative implementations of fault imaging via
109 seismic-waveform time reversal such as those by *Larmat et al.* [2006] and *Larmat et al.*
110 [2008] were successful from a theoretical standpoint, but seem too computationally heavy
111 for systematic practical application. Most seismologists only back-project seismogram peaks
112 associated with the arrival of P waves [e.g. *Ishii et al.*, 2005] so as to avoid costly simulations
113 of broad-band seismic-wave propagation in a heterogeneous, three-dimensional medium (the
114 Earth), whose heterogeneity is only approximately known. The only published experiment
115 in surface-wave back-projection that we are aware of is that of *Roten et al.* [2012]. While
116 the basic idea of *Roten et al.* [2012] is similar to some of the concepts presented here, their
117 approach is essentially a form of back-projection, with the inherent approximations.

118 We provide in sec. 2 a description of surface-wave propagation in terms of “potentials”
119 [e.g. *Udías*, 1999; *Aki and Richards*, 2002]. *Aki and Richards* [2002] state (box 7.5) that
120 “potentials are of no direct interest, and are awkward to use. . .”. We maintain that, as shown
121 e.g. by *Tanimoto* [1990] or *Peter et al.* [2007], there is interest in using potentials, particularly
122 for surface waves. For instance, if only the phase, and not the amplitude of the data is

123 studied, many useful applications (e.g., imaging, backward-propagation) become possible by
 124 using the potentials and the associated simple, two-dimensional (2-D) equations, without
 125 having to solve the more cumbersome radial equations, or the general three-dimensional
 126 equations. This is strictly true within a high-frequency approximation, but applications to
 127 real data have often shown that, in practice, this approximation works remarkably well. Our
 128 theoretical formulation in sec. 2 is different from that of *Aki and Richards* [2002] in that we
 129 use potentials, and from those of *Tanimoto* [1990] and *Tromp and Dahlen* [1993] in that we
 130 do not invoke variational principles.

131 The main implication of sec. 2 is that the scalar 2-D Helmholtz' equation can be used to
 132 model surface-wave propagation in a laterally smooth, lossless half space, confirming earlier
 133 results by *Tanimoto* [1990] and *Tromp and Dahlen* [1993]. In secs. 3 and 4 we accordingly
 134 derive the theory of time reversal in a 2-D "acoustic" medium (i.e., a medium whose defor-
 135 mations are described by the 2-D Helmholtz' equation). Finally (sec. 6), theoretical results
 136 are validated by direct application to synthetic and real surface-wave data. The applications
 137 presented here are limited to two-dimensions; in future work, we shall explore the resolving
 138 power of our method in the vertical direction, combining the results of multiple, Love- and
 139 Rayleigh-wave 2-D time-reversal simulations conducted at different frequencies.

140 2 Surface waves and the two-dimensional Helmholtz equation

141 The scalar 2-D Helmholtz' equation can be used to model surface-wave propagation in a
 142 laterally smooth, lossless half space. We shall give a simplified proof of this fundamental
 143 result by briefly summarizing some parts of earlier studies by *Tanimoto* [1990] and *Tromp*
 144 *and Dahlen* [1993]. Let us start by writing the displacement equation for an elastic, isotropic
 145 medium in the frequency (ω) domain [*Udías*, 1999, eq. (2.60)],

$$\frac{\partial}{\partial x_j} \left[\lambda \delta_{ij} \frac{\partial u_k}{\partial x_k} + \mu \left(\frac{\partial u_i}{\partial x_j} + \frac{\partial u_j}{\partial x_i} \right) \right] = -\rho \omega^2 u_j, \quad (1)$$

146 where x_1, x_2, x_3 are Cartesian coordinates, with the x_3 -axis perpendicular to Earth's surface
 147 (which we assume to be flat) and oriented downward; δ_{ij} is Kronecker's delta, ρ denotes
 148 density and λ, μ Lamé's parameters. Repeated indices are implicitly summed over. Following
 149 *Tanimoto* [1990], we assume the Earth to be smooth laterally (horizontal derivatives of ρ ,
 150 λ, μ , etc. are negligible) but not vertically (x_3 -derivatives of the same parameters are not
 151 negligible); eq. (1) then takes a slightly different form for $i=3$ with respect to $i=1,2$; namely

$$(\lambda + \mu) \frac{\partial}{\partial x_{1,2}} \left(\frac{\partial u_k}{\partial x_k} \right) + \mu \nabla^2 u_{1,2} + \frac{\partial \mu}{\partial x_3} \left(\frac{\partial u_{1,2}}{\partial x_3} + \frac{\partial u_3}{\partial x_{1,2}} \right) = -\rho \omega^2 u_{1,2}, \quad (2)$$

152 and

$$(\lambda + \mu) \frac{\partial}{\partial x_3} \left(\frac{\partial u_k}{\partial x_k} \right) + \mu \nabla^2 u_3 + 2 \frac{\partial \mu}{\partial x_3} \frac{\partial u_3}{\partial x_3} + \frac{\partial \lambda}{\partial x_3} \frac{\partial u_k}{\partial x_k} = -\rho \omega^2 u_3. \quad (3)$$

153 The displacement equations (1) or (2) and (3) are accompanied by the requirement that
 154 no tractions exist on the outer surface of the Earth ("free surface" boundary conditions); for

155 an isotropic elastic medium, the stress tensor

$$\sigma_{ij} = \lambda \frac{\partial u_k}{\partial x_k} \delta_{ij} + 2\mu \left(\frac{\partial u_i}{\partial x_j} + \frac{\partial u_j}{\partial x_i} \right), \quad (4)$$

156 and the zero-traction requirement at the outer (horizontal) surface is equivalent to requiring
 157 that $\sigma_{13}=\sigma_{23}=\sigma_{33}=0$ when $x_3=0$. Displacements and stresses are also usually required to be
 158 continuous across all discontinuities.

159 We next introduce a Rayleigh-wave displacement *Ansatz* in the frequency domain,

$$\mathbf{u}_R = U(x_3, \omega) \mathbf{x}_3 \phi_R(x_1, x_2, \omega) + V(x_3, \omega) \nabla_1 \phi_R(x_1, x_2, \omega), \quad (5)$$

160 where the unit-vectors $\mathbf{x}_1, \mathbf{x}_2, \mathbf{x}_3$ are parallel to the Cartesian axes, and $\nabla_1 = \mathbf{x}_1 \frac{\partial}{\partial x_1} + \mathbf{x}_2 \frac{\partial}{\partial x_2}$.
 161 The functions $U(x_3, \omega)$ and $V(x_3, \omega)$ control the dependence of surface-wave amplitude on
 162 depth; they do not need to be known explicitly at this stage. The function ϕ_R can be thought
 163 of as a ‘‘Rayleigh-wave potential’’. For Love waves,

$$\mathbf{u}_L = W(x_3, \omega) (-\mathbf{x}_3 \times \nabla_1) \phi_L(x_1, x_2, \omega), \quad (6)$$

164 with ϕ_L the ‘‘Love-wave potential’’, and $W(x_3, \omega)$ playing the same role as U and V above.
 165 It can be seen by inspection of expressions (5) and (6) that they indeed describe Rayleigh-
 166 and Love-wave motion, respectively. The functions U, V, W need not be specified at this
 167 point, but, if only surface-wave solutions are of interest, it must be required that

$$\lim_{x_3 \rightarrow \infty} U(x_3, \omega) = 0; \quad \lim_{x_3 \rightarrow \infty} V(x_3, \omega) = 0; \quad \lim_{x_3 \rightarrow \infty} W(x_3, \omega) = 0. \quad (7)$$

168 We next use our surface-wave *Ansätze* (5) and (6), together with the mentioned boundary
 169 conditions, to simplify and solve the displacement equations (2) and (3).

170 2.1 Love waves

171 We first substitute \mathbf{u} in eqs. (2), (3) with the expression (6) for \mathbf{u}_L . It is useful to notice that
 172 the \mathbf{x}_3 -component of \mathbf{u}_L is 0, and that \mathbf{u}_L is divergence-free; as a result, eq. (3) is always
 173 verified by \mathbf{u}_L as given by (6), whatever the functions $W(x_3)$ and $\phi_L(x_1, x_2)$. After some
 174 algebra, the remaining equations are reduced to

$$\left(\mu \frac{\partial^2 W}{\partial x_3^2} + \frac{\partial \mu}{\partial x_3} \frac{\partial W}{\partial x_3} + \rho \omega^2 W \right) \frac{\partial \phi_L}{\partial x_2} + \mu W \left(\frac{\partial^3 \phi_L}{\partial x_1^2 \partial x_2} + \frac{\partial^3 \phi_L}{\partial x_2^3} \right) = 0, \quad (8)$$

$$\left(\mu \frac{\partial^2 W}{\partial x_3^2} + \frac{\partial \mu}{\partial x_3} \frac{\partial W}{\partial x_3} + \rho \omega^2 W \right) \frac{\partial \phi_L}{\partial x_1} + \mu W \left(\frac{\partial^3 \phi_L}{\partial x_2^2 \partial x_1} + \frac{\partial^3 \phi_L}{\partial x_1^3} \right) = 0. \quad (9)$$

176 Remember that ϕ_L is only a function of x_1, x_2 , while $\mu = \mu(x_3), \rho = \rho(x_3)$ and $W = W(x_3)$.
 177 If we divide eq. (8) by $\mu W \frac{\partial \phi_L}{\partial x_2}$ we find

$$\frac{\mu \frac{\partial^2 W}{\partial x_3^2} + \frac{\partial \mu}{\partial x_3} \frac{\partial W}{\partial x_3} + \rho \omega^2 W}{\mu W} = - \frac{\frac{\partial^3 \phi_L}{\partial x_1^2 \partial x_2} + \frac{\partial^3 \phi_L}{\partial x_2^3}}{\frac{\partial \phi_L}{\partial x_2}}, \quad (10)$$

178 which can be solved by separation of variables [e.g. *Tromp and Dahlen*, 1993, sec. 3] since
 179 the right-hand side depends only on x_1 , x_2 , and the left-hand side only on x_3 . This means
 180 that we can introduce a constant k_L such that

$$\mu \frac{\partial^2 W}{\partial x_3^2} + \frac{\partial \mu}{\partial x_3} \frac{\partial W}{\partial x_3} + \rho \omega^2 W = \mu k_L^2 W \quad (11)$$

181 and

$$\frac{\partial^3 \phi_L}{\partial x_1^2 \partial x_2} + \frac{\partial^3 \phi_L}{\partial x_2^3} = -k_L^2 \frac{\partial \phi_L}{\partial x_2}. \quad (12)$$

182 It might be noticed that the “radial” eq. (11) is equivalent to equation (46) of *Takeuchi*
 183 *and Saito* [1972], or eq. (7.24) of *Aki and Richards* [2002], even though those treatments are
 184 limited to plane waves (which affects ϕ_L but not W).

185 Applying the same procedure to eq. (9) additionally gives

$$\frac{\partial^3 \phi_L}{\partial x_1 \partial x_2^2} + \frac{\partial^3 \phi_L}{\partial x_1^3} = -k_L^2 \frac{\partial \phi_L}{\partial x_1}, \quad (13)$$

186 and a sufficient condition for ϕ_L to solve both (12) and (13) is the Helmholtz’ equation

$$\frac{\partial^2 \phi_L}{\partial x_1^2} + \frac{\partial^2 \phi_L}{\partial x_2^2} = -k_L^2 \phi_L. \quad (14)$$

187 The boundary conditions can also be simplified when applied to our Love-wave *Ansatz*:
 188 it follows from (4) and (6) that, for Love waves, $\sigma_{33}=0$, and $\sigma_{13} = -\sigma_{23} = \mu \frac{\partial W}{\partial x_3} \frac{\partial \phi_L}{\partial x_1}$. The
 189 zero-traction boundary condition at the outer surface thus reduces to

$$\frac{\partial W}{\partial x_3} = 0 \text{ at } x_3 = 0. \quad (15)$$

190 2.1.1 Love-wave radial equation

191 Several different approaches to the (semi-analytical or numerical) solution of the “radial”
 192 equation (11) are reviewed in sections 7.1 and 7.2 of *Aki and Richards* [2002], starting with
 193 a simple one-layer-over-half-space model and then generalizing to the cases of an arbitrary
 194 number of layers, and of continuous velocity and density profiles. We need not repeat here
 195 the detailed treatment of *Aki and Richards* [2002], but it is useful to point out some of its
 196 essential implications.

197 Equation (11) is a second-order ordinary differential equation, whose general solution thus
 198 contains two arbitrary constants. Two boundary conditions must be taken into account: eqs.
 199 (7) and (15). These two equations allow in principle to determine both arbitrary constants.

200 If the Earth is modeled as a set of one or more uniform, horizontal layers overlying a half
 201 space, then within each layer i we have $\frac{\partial \mu}{\partial x_3} = 0$, and eq. (11) is simplified to the Helmholtz’
 202 equation

$$\frac{\partial^2 W}{\partial x_3^2} + (\rho_i \omega^2 - \mu_i k_L^2) W = 0, \quad (16)$$

203 where ρ_i and μ_i denote the (constant) values of density and rigidity within layer i , respectively.
 204 Each layer adds one second-order equation, and therefore two arbitrary constants to the
 205 problem, but also one interface with the associated two continuity conditions (on W and

206 $\frac{\partial W}{\partial x_3}$): again, all arbitrary constants can be determined.

207 The parameters ω and k_L , however, have not been specified, and, as a consequence,
208 one cannot simply identify a unique solution for W to be substituted into the *Ansatz* (6).
209 According to *Aki and Richards* [2002], this problem is solved in general as follows: (i) a
210 numerical value ω_0 is assigned to ω ; (ii) a numerical, “trial” value is likewise assigned to k_L ;
211 (iii) the selected numerical values ω_0 and k_L are substituted into eq. (11) which can then be
212 integrated numerically, or via the “propagator matrix” method [e.g. *Aki and Richards*, 2002,
213 sec. 7.2.2], starting with $W=0$ at large depth x_3 ; (iv) it is verified whether condition (15) is
214 met at $x_3=0$; (v) if this condition is not met, eq. (11) is integrated again, with the same ω_0
215 but a different trial value for k_L ; (vi) if, instead, the condition (15) is met, the whole process
216 is repeated for a new value ω_0 , until the frequency range of interest is entirely covered.

217 It is found that a discrete set of one or more (depending on ω_0) values of k_L for which the
218 free-surface boundary condition is met can be determined [e.g. *Aki and Richards*, 2002, figures
219 7.2, 7.3]. These values are dubbed “eigenvalues” in analogy with free-oscillation theory, and
220 each corresponds to a different solution, or “mode,” for W . If more than one eigenvalue exist
221 at a given frequency, the mode corresponding to the largest k_L eigenvalue is referred to as
222 “fundamental mode,” followed by “higher modes” (“overtones”).

223 2.1.2 Helmholtz’ equation for the Love-wave potential ϕ_L

224 The parameters k_L and ω in eq. (14) must be substituted with one of the eigenvalues of
225 k_L , and with the corresponding value ω_0 , respectively, before this equation is solved for ϕ_L .
226 Substitution of $\phi_L(x_1, x_2, \omega_0)$ and of the corresponding $W(x_3, \omega_0)$ into expression (6) yields
227 a monochromatic Love-wave solution. The process can be iterated at each frequency ω_0
228 for which the eigenvalues k_L and eigenfunctions W have been determined as described in
229 sec. 2.1.1.

230 Notice that, for a monochromatic wave of frequency ω_0 , eq. (14) coincides with the 2-D
231 wave equation with wavespeed $\frac{\omega_0}{k_L}$. The curve $k_L = k_L(\omega_0)$ is thus the “dispersion curve”
232 describing how surface-wave phase velocity depends on frequency.

233 It is easy to show that a monochromatic *plane* wave ϕ_L would solve eq. (14), and in fact
234 most seismology textbooks replace ϕ_L (and ϕ_R) with plane-wave formulae in the surface-
235 wave *Ansätze* [e.g. *Aki and Richards*, 2002]. In view of the applications to be discussed here,
236 however, circular (cylindrical) surface waves are more relevant. This case can be described, in
237 our formulation, starting with the known solution G_{2D} to the Green’s problem associated with
238 equation (14), obtained, e.g., in Appendix E of *Boschi and Weemstra* [2015]; $G_{2D}(x_1, x_2, \omega)$
239 is clearly not a monochromatic wave, but the response of the medium to a monochromatic
240 point source can be obtained, according to eq. (E34) of *Boschi and Weemstra* [2015], by time-
241 domain convolution or frequency-domain multiplication of $G_{2D}(x_1, x_2, \omega)$ with a sinusoidal
242 signal $\delta(\omega - \omega_0)$.

2.2 Rayleigh waves

In analogy with section 2.1, we next substitute \mathbf{u} in eqs. (2), (3) with the expression (5) for \mathbf{u}_R . This results, after some algebra, in the system of equations

$$\left[\mu \frac{\partial^2 V}{\partial x_3^2} + \frac{\partial \mu}{\partial x_3} \left(U + \frac{\partial V}{\partial x_3} \right) + (\lambda + \mu) \frac{\partial U}{\partial x_3} + \rho \omega^2 V \right] \frac{\partial \phi_R}{\partial x_1} + (\lambda + 2\mu) V \left(\frac{\partial^3 \phi_R}{\partial x_1^3} + \frac{\partial^3 \phi_R}{\partial x_2^2 \partial x_1} \right) = 0, \quad (17)$$

$$\left[\mu \frac{\partial^2 V}{\partial x_3^2} + \frac{\partial \mu}{\partial x_3} \left(U + \frac{\partial V}{\partial x_3} \right) + (\lambda + \mu) \frac{\partial U}{\partial x_3} + \rho \omega^2 V \right] \frac{\partial \phi_R}{\partial x_2} + (\lambda + 2\mu) V \left(\frac{\partial^3 \phi_R}{\partial x_2^3} + \frac{\partial^3 \phi_R}{\partial x_1^2 \partial x_2} \right) = 0, \quad (18)$$

$$\left[(\lambda + 2\mu) \frac{\partial^2 U}{\partial x_3^2} + 2 \frac{\partial \mu}{\partial x_3} \frac{\partial U}{\partial x_3} + \frac{\partial \lambda}{\partial x_3} \frac{\partial U}{\partial x_3} + \rho \omega^2 U \right] \phi_R + \left[(\lambda + \mu) \frac{\partial V}{\partial x_3} + \frac{\partial \lambda}{\partial x_3} V + \mu U \right] \left(\frac{\partial^2 \phi_R}{\partial x_1^2} + \frac{\partial^2 \phi_R}{\partial x_2^2} \right) = 0, \quad (19)$$

which, again, can be solved by the method of separation of variables. After dividing it by $(\lambda + \mu) \frac{\partial V}{\partial x_3} + \frac{\partial \lambda}{\partial x_3} V + \mu U$, eq. (19) can be separated into

$$(\lambda + 2\mu) \frac{\partial^2 U}{\partial x_3^2} + 2 \frac{\partial \mu}{\partial x_3} \frac{\partial U}{\partial x_3} + \frac{\partial \lambda}{\partial x_3} \frac{\partial U}{\partial x_3} + \rho \omega^2 U = k_R^2 \left[(\lambda + \mu) \frac{\partial V}{\partial x_3} + \frac{\partial \lambda}{\partial x_3} V + \mu U \right] \quad (20)$$

and the Helmholtz' equation

$$\frac{\partial^2 \phi_R}{\partial x_1^2} + \frac{\partial^2 \phi_R}{\partial x_2^2} = -k_R^2 \phi_R, \quad (21)$$

where k_R is, at this point, an arbitrary constant. If one then substitutes eq. (21) into (17) and (18), it becomes apparent that a sufficient condition for both of them to be solved is given by

$$(\lambda + \mu) \frac{\partial U}{\partial x_3} + \mu \frac{\partial^2 V}{\partial x_3^2} + \frac{\partial \mu}{\partial x_3} \left(U + \frac{\partial V}{\partial x_3} \right) + \rho \omega^2 V - k_R^2 (\lambda + 2\mu) V = 0. \quad (22)$$

The ‘‘radial’’ eqs. (20) and (22) form a linear system of second-order ordinary differential equations that can be solved to determine U and V . Since two equations and two unknown functions are now involved, the solution is more cumbersome, but qualitatively similar to the Love-wave case of sec. 2.1.1. Again, as shown by *Takeuchi and Saito* [1972] and *Aki and Richards* [2002] for the plane-wave case, a set of Rayleigh-wave ‘‘modes’’ can be found by numerical integration: each mode is defined by a frequency ω_0 and a value of k_R for which (20) and (22) are solved, and the boundary conditions met. The definitions of fundamental mode and overtone given in sec. 2.1.1 naturally holds also for Rayleigh waves.

The discussion of sec. 2.1.2 on the Love-wave potential ϕ_L also applies to the Rayleigh-wave potential ϕ_R , which is controlled by the Helmholtz' equation (21); in analogy with sec. 2.1.2, k_R can be interpreted as the ratio between the frequency and phase velocity of the corresponding Rayleigh-wave mode.

3 Reciprocity theorem in two dimensions

Consider the non-homogeneous 2-D Helmholtz' equation

$$\nabla_1^2 p(x_1, x_2, \omega) + \frac{\omega^2}{c^2} p(x_1, x_2, \omega) = -i\omega q(x_1, x_2, \omega), \quad (23)$$

268 where p could represent the displacement of a stretched membrane (whose density and tension
 269 determine the parameter c), and the forcing term $-\mathrm{i}\omega q$ a pressure exerted on the membrane
 270 per unit of surface density [e.g., *Kinsler et al.*, 1999, secs. 4.2 and 4.8]. Here and in the
 271 following we denote by $f(\omega)$ the Fourier transform of a generic function $f(t)$, and by i the
 272 imaginary unit. The following mathematical treatment makes it convenient to denote forcing
 273 as $-\mathrm{i}\omega q(x_1, x_2, \omega)$.

274 Let us define a vector $\mathbf{v} = -\frac{1}{\mathrm{i}\omega}\nabla_1 p$, such that

$$\nabla_1 p + \mathrm{i}\omega\mathbf{v} = \mathbf{0}. \quad (24)$$

275 Substituting eq. (24) into (23), we then find

$$\nabla_1 \cdot \mathbf{v} + \frac{\mathrm{i}\omega}{c^2}p - q = 0. \quad (25)$$

276 The following treatment follows closely that of *Boschi and Weemstra* [2015], who sum-
 277 marized earlier results by, e.g., *Wapenaar and Fokkema* [2006] and *Snieder* [2007], limited to
 278 three-dimensional space. Let us consider a surface S bounded by the closed curve ∂S . (∂S
 279 is just an arbitrary closed curve within a 2-D medium, and generally does not represent a
 280 physical boundary.) Let $q_A(x_1, x_2, \omega)$, $p_A(x_1, x_2, \omega)$ and $\mathbf{v}_A(x_1, x_2, \omega)$ denote a possible com-
 281 bination of the fields q , p and \mathbf{v} co-existing at (x_1, x_2) in S and ∂S . A different forcing q_B
 282 would give rise, through eqs. (24) and (25), to a different “state” B , defined by $p_B(x_1, x_2, \omega)$
 283 and $\mathbf{v}_B(x_1, x_2, \omega)$.

284 A useful relationship between the states A and B , known as “reciprocity theorem”, is
 285 obtained by combining eqs. (24) and (25) as follows,

$$\int_S \mathrm{d}^2\mathbf{x} [(24)_A \cdot \mathbf{v}_B^* + (24)_B^* \cdot \mathbf{v}_A + (25)_A p_B^* + (25)_B^* p_A] = 0, \quad (26)$$

286 where $\mathbf{x}=(x_1, x_2)$, $\mathrm{d}^2\mathbf{x} = \mathrm{d}x_1\mathrm{d}x_2$, and $*$ denotes complex conjugation. $(24)_A$ is short for the
 287 expression one obtains after substituting $p = p_A(\mathbf{x}, \omega)$ and $\mathbf{v} = \mathbf{v}_A(\mathbf{x}, \omega)$ into the left-hand
 288 side of eq. (24), etc. Namely,

$$(24)_A \cdot \mathbf{v}_B^* = \nabla_1 p_A \cdot \mathbf{v}_B^* + \mathrm{i}\omega\mathbf{v}_A \cdot \mathbf{v}_B^* \quad (27)$$

289

$$(24)_B^* \cdot \mathbf{v}_A = \nabla_1 p_B^* \cdot \mathbf{v}_A - \mathrm{i}\omega\mathbf{v}_B^* \cdot \mathbf{v}_A \quad (28)$$

290

$$(25)_A p_B^* = \nabla_1 \cdot \mathbf{v}_A p_B^* + \frac{\mathrm{i}\omega}{c^2}p_A p_B^* - q_A p_B^* \quad (29)$$

291

$$(25)_B^* p_A = \nabla_1 \cdot \mathbf{v}_B^* p_A - \frac{\mathrm{i}\omega}{c^2}p_B^* p_A - q_B^* p_A. \quad (30)$$

292 After substituting expressions (27) through (30) into eq. (26), the latter simplifies to

$$\int_S \mathrm{d}^2\mathbf{x} (\nabla_1 p_A \cdot \mathbf{v}_B^* + \nabla_1 p_B^* \cdot \mathbf{v}_A + \nabla_1 \cdot \mathbf{v}_A p_B^* + \nabla_1 \cdot \mathbf{v}_B^* p_A) = \int_S \mathrm{d}^2\mathbf{x} (q_A p_B^* + q_B^* p_A). \quad (31)$$

293 The integrand at the left-hand side of (31) can be further simplified via the relationship
 294 $\nabla_1 \cdot (p_A \mathbf{v}_B^*) = \nabla_1 p_A \cdot \mathbf{v}_B^* + \nabla_1 \cdot \mathbf{v}_B^* p_A$ (which naturally holds also if A and B are swapped).
 295 We next apply the 2-D version of the divergence theorem to the resulting expression, and eq.

296 (31) collapses to

$$\int_{\partial S} d\mathbf{x} (p_A \mathbf{v}_B^* + p_B^* \mathbf{v}_A) \cdot \mathbf{n} = \int_S d^2\mathbf{x} (q_A p_B^* + q_B^* p_A), \quad (32)$$

297 where \mathbf{n} is a unit vector everywhere perpendicular to ∂S . For instance, “Green’s identity”
 298 (4.22) of *Baker and Copson* [1950], or the “reciprocity theorem of the correlation type”, eq.
 299 (5) of *Wapenaar and Fokkema* [2006], are three-dimensional versions of eq. (32).

300 3.1 Application of the reciprocity theorem to impulsive point sources: ex- 301 act equations

302 Let us next consider the states A and B resulting from the impulsive forcing terms $q_A =$
 303 $\delta(\mathbf{x} - \mathbf{x}_A)$ and $q_B = \delta(\mathbf{x} - \mathbf{x}_B)$, respectively, with $\mathbf{x}_A, \mathbf{x}_B$ two arbitrary locations on S . It
 304 follows that $p_A = \mathcal{G}_{2D}(\mathbf{x}, \mathbf{x}_A, \omega)$ and $p_B = \mathcal{G}_{2D}(\mathbf{x}, \mathbf{x}_B, \omega)$, with \mathcal{G}_{2D} the Green’s function
 305 corresponding to a 2-D membrane excited by a nonzero right-hand side in eq. (23), and eq.
 306 (24) then implies that $\mathbf{v}_{A,B} = -\frac{1}{i\omega} \nabla_1 \mathcal{G}_{2D}(\mathbf{x}, \mathbf{x}_{A,B}, \omega)$.

307 \mathcal{G}_{2D} is the solution of the non-homogeneous eq. (23) with $q = \delta(\mathbf{x} - \mathbf{x}_{A,B})$. Based on eq.
 308 (E34) of *Boschi and Weemstra* [2015],

$$\begin{aligned} \mathcal{G}_{2D}(\mathbf{x}, \mathbf{x}_{A,B}, \omega) &= \int_{\mathbb{R}^2} d^2\mathbf{x}' G_{2D}(\mathbf{x}, \mathbf{x}', \omega) (-i\omega) \delta(\mathbf{x}' - \mathbf{x}_{A,B}) \\ &= -i\omega G_{2D}(\mathbf{x}, \mathbf{x}_{A,B}, \omega), \end{aligned} \quad (33)$$

309 where $G_{2D}(\mathbf{x}, \mathbf{x}', \omega)$ is the Green’s function associated with a nonzero *initial velocity* at \mathbf{x}' ,
 310 derived explicitly e.g. by *Boschi and Weemstra* [2015]. To translate the time-domain formula
 311 of *Boschi and Weemstra* [2015] into frequency domain, it is useful to notice that eq. (E34)
 312 of *Boschi and Weemstra* [2015] involves the time-domain convolution of G_{2D} with the non-
 313 homogeneous term (forcing term) of the wave equation, and to remember that a convolution
 314 in the time-domain maps to a product in the frequency domain.

315 Replacing $p_{A,B}$ and $\mathbf{v}_{A,B}$ in eq. (32) with their expressions in terms of G_{2D} , and $q_{A,B}$
 316 with a Dirac delta,

$$\begin{aligned} &G_{2D}^*(\mathbf{x}_A, \mathbf{x}_B, \omega) - G_{2D}(\mathbf{x}_B, \mathbf{x}_A, \omega) \\ &= \int_{\partial S} d\mathbf{x}' [G_{2D}^*(\mathbf{x}', \mathbf{x}_B, \omega) \nabla_1 G_{2D}(\mathbf{x}', \mathbf{x}_A, \omega) - G_{2D}(\mathbf{x}', \mathbf{x}_A, \omega) \nabla_1 G_{2D}^*(\mathbf{x}', \mathbf{x}_B, \omega)] \cdot \mathbf{n}. \end{aligned} \quad (34)$$

317 Eq. (34) can be thought of as the 2-D version of eq. (19) in *Wapenaar and Fokkema* [2006]
 318 or eq. (96) in *Boschi and Weemstra* [2015].

319 The above treatment holds if \mathbf{x}_A and \mathbf{x}_B are not within S ; in that case, $q_{A,B}$ are zero
 320 within S . The integral at the right-hand side of eq. (32) is therefore zero, and so is, as a
 321 result, the left-hand side of (34). It follows that the integral at the right-hand side of (34) is
 322 zero if \mathbf{x}_A and \mathbf{x}_B are not within S [*Baker and Copson*, 1950, sec. 6.2].

3.2 Application of the reciprocity theorem to impulsive point sources: far-field/high-frequency approximation

Equation (34) can be simplified by the “far-field” approximation, which requires that the locations \mathbf{x}_A and \mathbf{x}_B be separated from one another and from ∂S by at least a few wavelengths. We additionally require that $\mathbf{x} - \mathbf{x}_A \approx \mathbf{x} - \mathbf{x}_B$ for any point \mathbf{x} on ∂S (i.e., \mathbf{x}_A and \mathbf{x}_B are both very far from ∂S). The Green’s function G_{2D} can be replaced by its far-field approximation, which reads

$$G_{2D}(\mathbf{x}, \mathbf{y}, \omega) \approx \frac{1}{4i\pi c^{3/2}} \frac{e^{-i\left(\frac{\omega|\mathbf{x}-\mathbf{y}|}{c} - \frac{\pi}{4}\right)}}{\sqrt{\omega|\mathbf{x}-\mathbf{y}|}} \quad (35)$$

[e.g., *Boschi and Weemstra*, 2015, eq. (E17)]. We next take advantage of this approximation to find a simple expression for $\nabla_1 G_{2D}$. Let us consider for example $\nabla_1 G_{2D}(\mathbf{x}, \mathbf{x}_A, \omega)$ and call $r = |\mathbf{x} - \mathbf{x}_A|$. Then,

$$\begin{aligned} \nabla_1 G_{2D}(\mathbf{x}, \mathbf{x}_A, \omega) &\approx \frac{1}{4i\pi c^{3/2}} \left(\mathbf{x}_1 \frac{\partial}{\partial x_1} + \mathbf{x}_2 \frac{\partial}{\partial x_2} \right) \left[\frac{e^{-i\left(\frac{\omega r}{c} - \frac{\pi}{4}\right)}}{\sqrt{\omega r}} \right] \\ &= \frac{1}{4i\pi c^{3/2}} \left(\mathbf{x}_1 \frac{\partial r}{\partial x_1} + \mathbf{x}_2 \frac{\partial r}{\partial x_2} \right) \frac{\partial}{\partial r} \left[\frac{e^{-i\left(\frac{\omega r}{c} - \frac{\pi}{4}\right)}}{\sqrt{\omega r}} \right] \\ &= \frac{1}{4i\pi c^{3/2}} \left[\frac{i\omega}{c} + \frac{1}{2r} \right] \frac{e^{-i\left(\frac{\omega r}{c} - \frac{\pi}{4}\right)}}{\sqrt{\omega r}} \nabla_1 r \\ &= G_{2D}(\mathbf{x}, \mathbf{x}_A, \omega) \left[\frac{i\omega}{c} + \frac{1}{2r} \right] \nabla_1 r. \end{aligned} \quad (36)$$

In the far-field approximation, r is large and r^{-1} is much larger than r^{-2} : the second term inside square brackets in eq. (36) can be neglected. If one takes the origin, e.g., at \mathbf{x}_A , the condition $\mathbf{x} - \mathbf{x}_A \approx \mathbf{x} - \mathbf{x}_B$ implies that both $\mathbf{x} - \mathbf{x}_A$ and $\mathbf{x} - \mathbf{x}_B$ can be replaced by \mathbf{x} , and $\nabla_1 r \approx \frac{\mathbf{x}}{|\mathbf{x}|}$. We are left with

$$\nabla_1 G_{2D}(\mathbf{x}, \mathbf{x}_A, \omega) \approx \frac{i\omega}{c} G_{2D}(\mathbf{x}, \mathbf{x}_A, \omega) \frac{\mathbf{x}}{|\mathbf{x}|}, \quad (37)$$

which we can finally substitute into eq. (34), to find

$$\begin{aligned} &G_{2D}^*(\mathbf{x}_A, \mathbf{x}_B, \omega) - G_{2D}(\mathbf{x}_B, \mathbf{x}_A, \omega) \\ &\approx \frac{i\omega}{c} \int_{\partial S} d\mathbf{x}' \left[G_{2D}(\mathbf{x}', \mathbf{x}_A, \omega) G_{2D}^*(\mathbf{x}', \mathbf{x}_B, \omega) + G_{2D}^*(\mathbf{x}', \mathbf{x}_B, \omega) G_{2D}(\mathbf{x}', \mathbf{x}_A, \omega) \right] \frac{\mathbf{x}'}{|\mathbf{x}'|} \cdot \mathbf{n}. \end{aligned} \quad (38)$$

Remember that the closed curve ∂S does not correspond to a physical boundary. We choose it to be circular (we shall see in the following that this assumption does not affect the relevant physical interpretations of our results), so that $\frac{\mathbf{x}}{|\mathbf{x}|} = \mathbf{n}$ on ∂S . Eq. (38) collapses to

$$G_{2D}^*(\mathbf{x}_A, \mathbf{x}_B, \omega) - G_{2D}(\mathbf{x}_B, \mathbf{x}_A, \omega) \approx \frac{2i\omega}{c} \int_{\partial S} d\mathbf{x}' G_{2D}(\mathbf{x}', \mathbf{x}_A, \omega) G_{2D}^*(\mathbf{x}', \mathbf{x}_B, \omega), \quad (39)$$

which is the 2-D counterpart of eq. (102) in *Boschi and Weemstra* [2015]. (It is also consistent with eq. (65) of the same study, valid for a 2-D medium, derived via the stationary-phase approximation and setting source density to 1.)

4 Implications for surface waves: diffuse-field interferometry, time reversal

We know from sec. 2 that the Rayleigh- and Love-wave potentials ϕ_R , ϕ_L , just like the “membrane-wave” field p , obey the Helmholtz’ equation (23). It follows that eqs. (34) and (39) continue to be valid if p is replaced by potentials ϕ_R or ϕ_L , and if c is the Rayleigh- or Love-wave phase velocity at that frequency. We also know that the vertical displacement associated with a Rayleigh wave is proportional to ϕ_R and thus obeys (23) exactly at the frequency ω [e.g. *Boschi and Weemstra*, 2015]; slightly more complicated relations exist between Love-wave displacement (and the horizontal component of Rayleigh-wave displacement) and the Love-wave (Rayleigh-wave) potential, which are given e.g. by *Kaestle et al.* [2016]. In summary, the results of sec. 3 can be applied to the propagation of seismic surface waves, which will be the focus of the remainder of this study.

Eqs. (34) and its approximate version (39) describe the physics underlying both ambient-noise interferometry and acoustic/seismic time reversal. Analogies between these two techniques were first discussed by *Derode et al.* [2003].

4.1 Analogy with diffuse-field interferometry

In the context of diffuse-field interferometry, the far-field eq. (39) is invoked more often than its exact counterpart (34). The points \mathbf{x}_A , \mathbf{x}_B in eq. (39) are taken to represent the locations of two receivers, while the points on δS are thought of as point sources. The right-hand side of (39) is the cross-correlation of the signal recorded at receiver \mathbf{x}_A with that recorded at receiver \mathbf{x}_B , averaged (integrated, “stacked”...) over all sources. It is usually assumed that sources are approximately distributed along a closed curve surrounding the receivers in the far field. (If that is the case, it has also been shown that the cross-correlation of signals generated by different sources that act simultaneously will tend to cancel out; see *Boschi and Weemstra* [2015] for a more detailed discussion.) Eq. (39) then implies that the receiver-receiver cross-correlation at its right-hand side coincides approximately with the imaginary part of the frequency-domain Green’s function G_{2D} at the left-hand side. Since G_{2D} is real in the time-domain, and nonzero only at positive times, $G_{2D}(\mathbf{x}_A, \mathbf{x}_B, t)$ is determined without ambiguity by the imaginary part of its Fourier transform $G_{2D}(\mathbf{x}_A, \mathbf{x}_B, \omega)$ [*Boschi and Weemstra*, 2015]. It follows that the surface-wave Green’s function between two locations can be reconstructed from the cross-correlation of a diffuse surface-wave field recorded at those locations.

Recall now that, at the beginning of sec. 3.1, the assumption has been made that sources be impulsive. In practice, this amounts to selecting $q(\mathbf{x}, \omega) = \delta(\mathbf{x} - \mathbf{x}_{A,B})$, i.e., in the time domain, $q(\mathbf{x}, t) = \delta(\mathbf{x} - \mathbf{x}_{A,B})\delta(t)$. Let us next consider the case of arbitrary, unspecified time-dependence $h(t)$ of the source signal, i.e. $q(\mathbf{x}, t) = \delta(\mathbf{x} - \mathbf{x}_{A,B})h(t)$. Eq. (33) here was obtained from eq. (E34) of *Boschi and Weemstra* [2015], replacing the generic source signal there with the right-hand side of the non-homogeneous Helmholtz’ eq. (23). The solution p corresponding to an arbitrary source signal $h(t)$ is therefore obtained by updating the right-hand side of eq. (23), which in the frequency domain now reads $-i\omega\delta(\mathbf{x} - \mathbf{x}_{A,B})h(\omega)$. After substituting this into eq. (E34) of *Boschi and Weemstra* [2015], we find

$$p(\mathbf{x}, \mathbf{x}_{A,B}, \omega) = -i\omega G_{2D}(\mathbf{x}, \mathbf{x}_{A,B}, \omega)h(\omega), \quad (40)$$

384 which replaces our eq. (33).

385 Substituting (40) and $q(\mathbf{x}, \omega) = \delta(\mathbf{x} - \mathbf{x}_{A,B})h(\omega)$ into eqs. (24) and (32), we find that
 386 introducing the time-dependence $h(t)$ of the source boils down to multiplying both sides of
 387 eq. (34), and therefore (39), by the squared Fourier spectrum $|h(\omega)|^2$.

388 In ambient-noise interferometry, this means that if all noise sources had the same spec-
 389 trum then the cross-correlation of recorded ambient signal would also exhibit that spectrum
 390 (squared): consequently, we would not be reconstructing the Green’s function but rather its
 391 time-domain convolution with the source-related term $|h(\omega)|^2$. Indeed, it is well known that
 392 the spectrum of seismic ambient-noise cross correlation is dominated by peaks that corre-
 393 spond to the spectrum of oceanic microseisms [Longuet-Higgins, 1950; Stehly et al., 2006]. In
 394 many derivations of ambient-noise theory, the signals emitted by different noise sources are
 395 simply assumed to be random and uncorrelated, which results in the $|h(\omega)|^2$ factor canceling
 396 out [e.g. Campillo and Roux, 2014].

397 4.2 Surface-wave time reversal

398 If eq. (34) is to be used as an illustration of time-reversal acoustics [e.g., Fink, 1999], \mathbf{x}_B
 399 should be thought of as the location of a source; $G_{2D}(\mathbf{x}', \mathbf{x}_B, \omega)$ is the Fourier-transform of
 400 the signal generated at \mathbf{x}_B and recorded by a far-away receiver at \mathbf{x}' ; its complex-conjugate
 401 $G_{2D}^*(\mathbf{x}', \mathbf{x}_B, \omega)$ is the Fourier transform of the same signal, reversed in time. Imagine that
 402 the time-reversed signal be then emitted from \mathbf{x}' and recorded at another point \mathbf{x}_A : this
 403 amounts to convolving (in the frequency domain, multiplying) the time-reversed signal with
 404 the Green’s function $G_{2D}(\mathbf{x}_A, \mathbf{x}', \omega)$. Eq. (39) then shows that by repeating time reversal
 405 and propagation (“backward in time”) for all points \mathbf{x}' on ∂S and summing all the resulting
 406 traces at \mathbf{x}_B , the imaginary part of the Green’s function between \mathbf{x}_B and \mathbf{x}_A is obtained.

407 If ∂S is in the near field of \mathbf{x}_A , \mathbf{x}_B , the approximate eq. (39) should be replaced by
 408 (34), which is the 2-D version of eq. (3) in Fink [2006]. In practice, this means that to
 409 reconstruct the Green’s function between \mathbf{x}_A and \mathbf{x}_B one needs to (i) time-reverse (in the
 410 frequency domain, take the complex-conjugate of) the signal $G_{2D}(\mathbf{x}', \mathbf{x}_B, \omega)$ emitted by \mathbf{x}_B
 411 and recorded at \mathbf{x}' ; (ii) take the spatial derivative of the time-reversed signal in the \mathbf{n} direction
 412 at \mathbf{x}' , i.e. $\mathbf{n} \cdot \nabla_1 G_{2D}^*(\mathbf{x}', \mathbf{x}_B, \omega)$; (iii) convolve the time-reversed signal $G_{2D}^*(\mathbf{x}', \mathbf{x}_B, \omega)$ with
 413 the *dipole* response (see appendix) $\mathbf{n} \cdot \nabla_1 G_{2D}(\mathbf{x}_A, \mathbf{x}', \omega)$ between \mathbf{x}_A and \mathbf{x}' ; (iv) convolve its
 414 spatial-derivative with the impulse response between the same two points; (v) sum the two
 415 signals obtained at (iii) and (iv). In other words, rather than simply backward-propagating
 416 the signal recorded at receivers on ∂S , as in the far-field case, we must backward-propagate
 417 the sum of a dipole and a monopole source, to which the initial signal itself and its spatial
 418 derivative are “fed”, respectively.

419 The backward-propagated signal so obtained coincides, approximately (if eq. (39) is
 420 implemented) or exactly (eq. (34)), with the difference

$$G_{2D}^*(\mathbf{x}_A, \mathbf{x}_B, \omega) - G_{2D}(\mathbf{x}_B, \mathbf{x}_A, \omega) = -2i \Im [G_{2D}(\mathbf{x}_A, \mathbf{x}_B, \omega)]. \quad (41)$$

421 To understand the physical meaning of this expression, let us take its inverse Fourier transform
 422 (\mathcal{F}^{-1}). It follows from eqs. (B6) and (B9) of Boschi and Weemstra [2015] that

$$\mathcal{F}^{-1} \{-2i \Im [G_{2D}(\mathbf{x}_A, \mathbf{x}_B, \omega)]\} = G_{2D}(\mathbf{x}_A, \mathbf{x}_B, t) - G_{2D}(\mathbf{x}_A, \mathbf{x}_B, -t), \quad (42)$$

423 similar, e.g., to eq. (6) of *Fink* [2006]. Consider an arbitrary observation point \mathbf{x}_A within
 424 ∂S , and recall that G_{2D} is nonzero only at positive time. As t grows from $-\infty$ to 0, only
 425 the second term at the right-hand side of (42) is nonzero, which means that \mathbf{x}_A records a
 426 time-reversed Green's function. In space, a time-reversed impulsive circular wave converging
 427 towards the original source location \mathbf{x}_B is observed. As $t \rightarrow 0$, the value of \mathbf{x}_A for which the
 428 field is maximum approaches \mathbf{x}_B , where the backward-propagating circular wave eventually
 429 "focuses." As t grows from 0 to ∞ , only the first term at the right-hand side of (42) is nonzero,
 430 and \mathbf{x}_A records a regular Green's function with inverted sign. That is to say, another circular
 431 wave is emitted from \mathbf{x}_B after focusing.

432 In the words of *Fink* [2006], "if we were able to create a film of the propagation of the
 433 acoustic field during" propagation of the signal from the original source at \mathbf{x}_B to receivers
 434 on ∂S , "the final result could be interpreted as a projection of this film in the reverse order,
 435 immediately followed by a reprojection in the initial order." *Fink* [2006] notes that acoustic
 436 time reversal, as described here, does not involve the "time reversal of the source," and in
 437 "an ideal time-reversed experiment, the initial active source (that injects some energy into
 438 the system) must be replaced by a sink (the time reversal of a source)," i.e., "a device that
 439 absorbs all arriving energy without reflecting it."

440 Result (41) is limited to impulsive signals. If the signal emitted at \mathbf{x}_B is an arbitrary
 441 function of time, $h(t)$, the signal recorded at each receiver location \mathbf{x}' is the convolution
 442 $G_{2D}(\mathbf{x}', \mathbf{x}_B, \omega)h(\omega)$. Accordingly, let us replace $G_{2D}^*(\mathbf{x}', \mathbf{x}_B, \omega)$ at the right-hand side of eq.
 443 (34) with the convolution $G_{2D}^*(\mathbf{x}', \mathbf{x}_B, \omega)h^*(\omega)$. Since the function h does not depend on any
 444 other variable but t (or ω in the frequency domain), it can be pulled out of the \mathbf{x}' -integral; it
 445 then follows from eq. (34) itself that

$$\begin{aligned} & h^*(\omega) [G_{2D}^*(\mathbf{x}_A, \mathbf{x}_B, \omega) - G_{2D}(\mathbf{x}_B, \mathbf{x}_A, \omega)] \\ &= \int_{\partial S} d\mathbf{x}' \{ [h(\omega)G_{2D}(\mathbf{x}', \mathbf{x}_B, \omega)]^* \nabla_1 G_{2D}(\mathbf{x}', \mathbf{x}_A, \omega) - G_{2D}(\mathbf{x}', \mathbf{x}_A, \omega) \nabla_1 [h(\omega)G_{2D}(\mathbf{x}', \mathbf{x}_B, \omega)]^* \} \cdot \mathbf{n}. \end{aligned} \quad (43)$$

446 If one denotes $s(\mathbf{x}', \mathbf{x}_B, \omega) = h(\omega)G_{2D}(\mathbf{x}', \mathbf{x}_B, \omega)$, eq. (43) takes the more compact form

$$\begin{aligned} & h^*(\omega) [G_{2D}^*(\mathbf{x}_A, \mathbf{x}_B, \omega) - G_{2D}(\mathbf{x}_B, \mathbf{x}_A, \omega)] \\ &= \int_{\partial S} d\mathbf{x}' [s^*(\mathbf{x}', \mathbf{x}_B, \omega) \nabla_1 G_{2D}(\mathbf{x}', \mathbf{x}_A, \omega) - G_{2D}(\mathbf{x}', \mathbf{x}_A, \omega) \nabla_1 s^*(\mathbf{x}', \mathbf{x}_B, \omega)] \cdot \mathbf{n}. \end{aligned} \quad (44)$$

447 Alternatively, the far-field approximation (37) can be applied to (43), which, in analogy with
 448 sec. 3.1, collapses to

$$h^*(\omega) [G_{2D}^*(\mathbf{x}_A, \mathbf{x}_B, \omega) - G_{2D}(\mathbf{x}_B, \mathbf{x}_A, \omega)] \approx \frac{2i\omega}{c} \int_{\partial S} d\mathbf{x}' [s^*(\mathbf{x}', \mathbf{x}_B, \omega)G_{2D}(\mathbf{x}', \mathbf{x}_A, \omega)]. \quad (45)$$

449 Eqs. (44) and (45) stipulate that the same results obtained above for impulsive signals
 450 also apply to arbitrary signals $h(t)$, except that in this case the backward-propagating Green's
 451 function is convoluted with the time-reversed signal, $h^*(\omega)$ or $h(-t)$, itself. Importantly, the
 452 backward-propagating wave field focuses, again, on the source location \mathbf{x}_B .

5 Implementation

The so-called membrane-wave approach is based on the horizontal/radial decoupling of the equation of motion illustrated in sec. 2, where it is shown that the membrane eq. (23) holds for both the Love- and Rayleigh-wave potentials ϕ_L and ϕ_R . In sec. 3, some properties of the solution of (23), that naturally apply to both ϕ_R and ϕ_L , are derived. Their most important implication in the context of our study is explained in sec. 4: the theory of acoustic time reversal as developed by, e.g., *Fink* [2006] holds on a flat membrane, and, as a result, the time-reversed potentials ϕ_L , ϕ_R can be obtained from eqs. (44) or (45), i.e., by time-reversing and backward propagating the potentials associated with the recorded waveforms. Surface-wave time reversal then consists of (i) extracting ϕ_L and ϕ_R from the data, for a broad and dense set of surface-wave fundamental and higher modes; (ii) determining radial eigenfunctions (U and V , or W) for each mode; (iii) backward propagating ϕ_L and ϕ_R for each mode; (iv) combining potentials with radial eigenfunctions at all available frequencies, via eqs. (5) and (6), to find the time-reversed displacements \mathbf{u}_R and \mathbf{u}_L .

An important limitation of this procedure, as discussed in some detail in sec. 4.2, is that the time-reversed wave field necessarily includes an impulse propagating away from the reconstructed source location *after* focusing. This is not a problem for point sources (or of less-than-wavelength spatial extent, as in this study), but the time-reversed wave field at each point of a *finite-extent* source will include a non-physical contribution that cannot easily be subtracted from it, and that pollutes images of seismic slip. It should be noted that back-projection methods suffer from the same problem, although this is rarely (if ever) discussed. This issue will have to be addressed in future work. One possible strategy would be to subdivide the source-imaging process into two steps. First, time reversal could be interrupted before focusing occurs: this way, the surface-wave field in the immediate vicinity of the source could be reconstructed. In a second step, the reconstructed near-field displacement could be treated as data in a classic linear inverse problem, based on the representation theorem [e.g. *Ide*, 2007]: the unknown being slip on the fault. The accuracy of near-field displacement as reconstructed by time reversal would significantly reduce nonuniqueness.

Only monochromatic, fundamental-mode Rayleigh-wave propagation is implemented here. At each frequency of interest ω , propagation of the corresponding sinusoidal Rayleigh wave is modeled in the time domain. It is apparent from eq. (5) that, at frequency ω , ϕ_R is directly proportional to the vertical component of displacement, narrow-band-pass-filtered around ω ; i.e., before time reversal, $\phi_R(\omega)$ can be obtained by the vertical component of the displacement by simply multiplying it by $1/U(\omega)$. The implementation of time reversal is exactly the same for Love waves (except that membrane-wave propagation of the Love-wave potential must naturally be modeled in a Love-wave phase velocity map); the Love-wave potential ϕ_L , however, needs to be extracted from the *transverse* component of cross correlations, which will require some more subtle data processing to be addressed in future work.

Accordingly, we do not yet reconstruct time-reversed displacements from time-reversed potentials. This requires that the eigenfunctions U , V and W be computed for a selected reference model. Because the crust/lithosphere depth range (i.e., the depth range of interest to surface-wave propagation) is characterized by large lateral heterogeneity, it is likely that a 3-D reference model will need to be employed, through the implementation of “local” radial

497 eigenfunctions [e.g. *Boschi and Ekström*, 2002]. Studying the focusing of the Rayleigh-wave
498 vertical component at various frequencies is, however, sufficient to verify the feasibility of
499 our approach, which is the main goal of the present study. In the following, we model the
500 propagation of time-reversed surface-wave potentials via two different approaches: ray theory
501 and the spectral-element method.

502 In the ray-theory case, the value of G_{2D} for any given source and receiver position is
503 determined approximately by tracing the ray between source and receiver, computing the
504 propagation time along such ray path, and shifting by such time the signal prescribed at a
505 source. Rays are traced by means of the algorithm described by *Fang et al.* [2015]. Geo-
506 metrical spreading is accounted for approximately by simply multiplying the signal by the
507 inverse squared root of the source-receiver distance, according, e.g., to eq. (E17) of *Boschi*
508 *and Weemstra* [2015].

509 In the spectral-element case, following *Tape et al.* [2007], SPECFEM2D [*Komatitsch and*
510 *Tromp*, 1999] is used to simulate the propagation, on a stretched, flat membrane, of a dis-
511 placement perpendicular to the unperturbed membrane surface. Displacement is generated
512 by prescribing a point force/acoustic pressure (rather than an initial displacement as in
513 the ray-theory case), which implies, importantly, that our comparison between ray-theory
514 and SPECFEM2D results is only qualitative. Additionally, to model wave propagation via
515 SPECFEM2D, we need to project our spherical-Earth phase-velocity map onto a flat sur-
516 face. This is done via a transverse Mercator projection centered at 12°E, 46°N. Errors are
517 introduced near the corners of the region of interest, that will (slightly) alter modeled wave-
518 forms and might reduce the quality of focusing: the flat-membrane approach is adequate to
519 the feasibility study presented here, but curved membranes will have to be implemented for
520 future applications.

521 6 Validation

522 We test both ray-theory and spectral-element methods on synthetic membrane-wave data,
523 on ambient-noise vertical-component cross correlations (which are theoretically equivalent
524 to recordings of Rayleigh-wave impulse responses) and on vertical-component recordings of a
525 5.6-magnitude earthquake. To make sure that we can rely on robust, high-resolution Rayleigh-
526 wave phase-velocity maps and a dense station coverage, we select Northern Italy, including
527 most of the Alpine mountain range, as our study region. This area is characterized by complex
528 tectonics, and at this scale surface waves are difficult to identify as they are hidden in the
529 body-wave coda: if we can validate our theory in such an unfavorable situation, we can then
530 expect that it will hold also at teleseismic scales. Furthermore, by limiting the experiments
531 presented here to a relatively small region, we reduce the associated computational costs.

532 Earthquake data were downloaded from EIDA (<http://www.orfeus-eu.org/data/eida/>)
533 and from all permanent broadband stations that recorded the earthquake within the region
534 of interest; this includes INGV [*INGV Seismological Data Centre*, 1997], SED [*Swiss Seis-*
535 *mological Service (SED) at ETH Zurich*, 1983], OGS [*Istituto Nazionale di Oceanografia e di*
536 *Geofisica Sperimentale*, 2002], MedNet [*MedNet project partner institutions*, 1988] and the
537 University of Genova data archive. Continuous ambient data for the year 2010 were down-
538 loaded from all available permanent broadband stations that were active during that time,

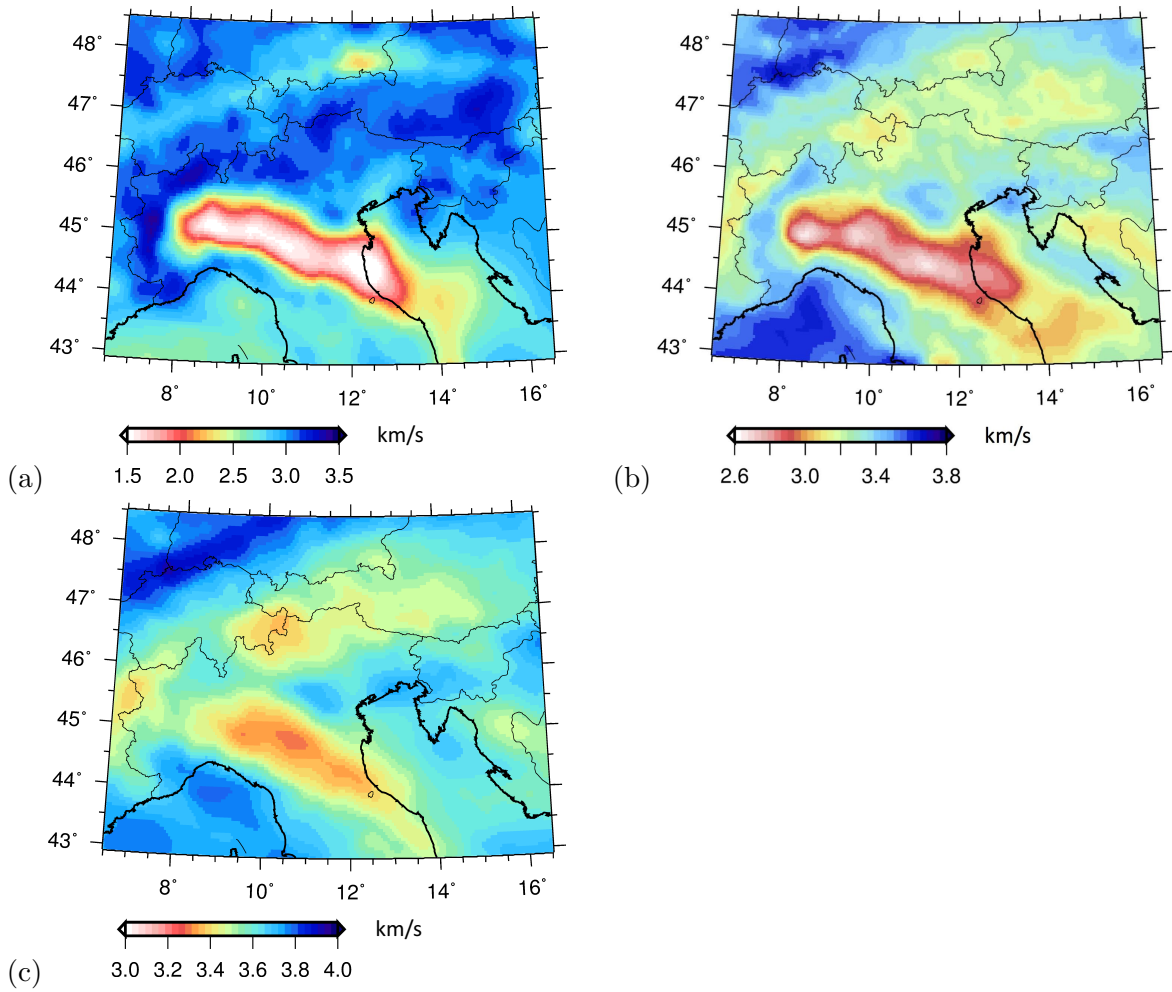


Figure 1: Rayleigh-wave phase-velocity maps of *Kaestle et al.* [2017], at periods of (a) 6 s, (b) 16 s and (c) 25 s.

539 via the INGV data center. Time-domain cross correlations were computed as described by
540 *Molinari et al.* [2018].

541 As a general rule, computational costs are much reduced with respect to typical 3-D wave-
542 propagation modeling applications in seismology. A time-reversal simulation, such as the ones
543 shown in the following, involves one single run of SPEC-FEM2D with multiple sources (one
544 per station), which requires about two hours on a single CPU. Ray-theory based simulations
545 are much cheaper: a time-reversal simulation can be completed in less than two minutes on
546 similar hardware.

547 6.1 Synthetic tests

548 Theoretical traces associated with a selected point-source location and a realistic station
549 distribution in the region of interest are obtained via ray theory and SPEC-FEM2D. The
550 source signal $h(t)$ is a Ricker wavelet as implemented in SPEC-FEM2D, Butterworth-filtered
551 between 6 and 26 s. Membrane waves are propagated through the 16s Rayleigh-wave phase-
552 velocity map of *Kaestle et al.* [2017], shown here in Fig. 1b. While only one particular
553 surface-wave mode is implemented for this synthetic test, it is understood that the exact same
554 procedure can be applied in the calculation of other Rayleigh- and Love-wave fundamental
555 modes and overtones. No random noise is added to the synthetic signal.

556 Because the station distribution is nonuniform, the curve ∂S and, as a consequence, the
557 vector \mathbf{n} in eq. (34) are not uniquely defined. We avoid this difficulty by replacing eq.
558 (34) with its far-field approximation (39), which can be implemented without specifying \mathbf{n} .
559 Preliminary experiments show that, despite the small size of the study region, the location of
560 the backward propagating wave field’s focus is not visibly affected by this approximation. We
561 plan to find ways to implement (34) exactly in future work, but we believe that the simplified
562 approach employed here is adequate to the scope of this article. We accordingly time-reverse
563 the traces, and propagate them backward in time, essentially implementing the right-hand
564 side of eq. (45). Again, waves are propagated through the map of Fig. 1b.

565 We obtain a pair of animations, one based on ray theory and the other on SPEC-FEM2D.
566 Samples of both are shown in Fig. 2. Fig. 3 shows the prescribed and reconstructed signal
567 at the known source location, again for both methods. While the backward propagating
568 wave fields differ because of the mentioned physical differences in the implementation (excitation
569 by initial displacement vs. point force, curved membrane vs. Mercator projection),
570 it appears from Fig. 2c,d that the maximum amplitude with respect to time and position
571 in both simulations corresponds to the known, initial source location. This confirms the
572 validity of surface-wave time reversal as a tool to localize/image a seismic source, despite
573 the severe nonuniformity in receiver distribution. The maximum is less pronounced in the
574 spectral-element simulation, resulting in normalized amplitudes throughout the simulation
575 to be larger than ray-theory-based amplitudes. After focusing, in the absence of an “acoustic
576 sink” (sec. 4.2), a non-physical wave field propagates away from the source. There are
577 no major differences in the quality of focusing achieved by ray-theory vs. SPEC-FEM2D
578 backward-propagation.

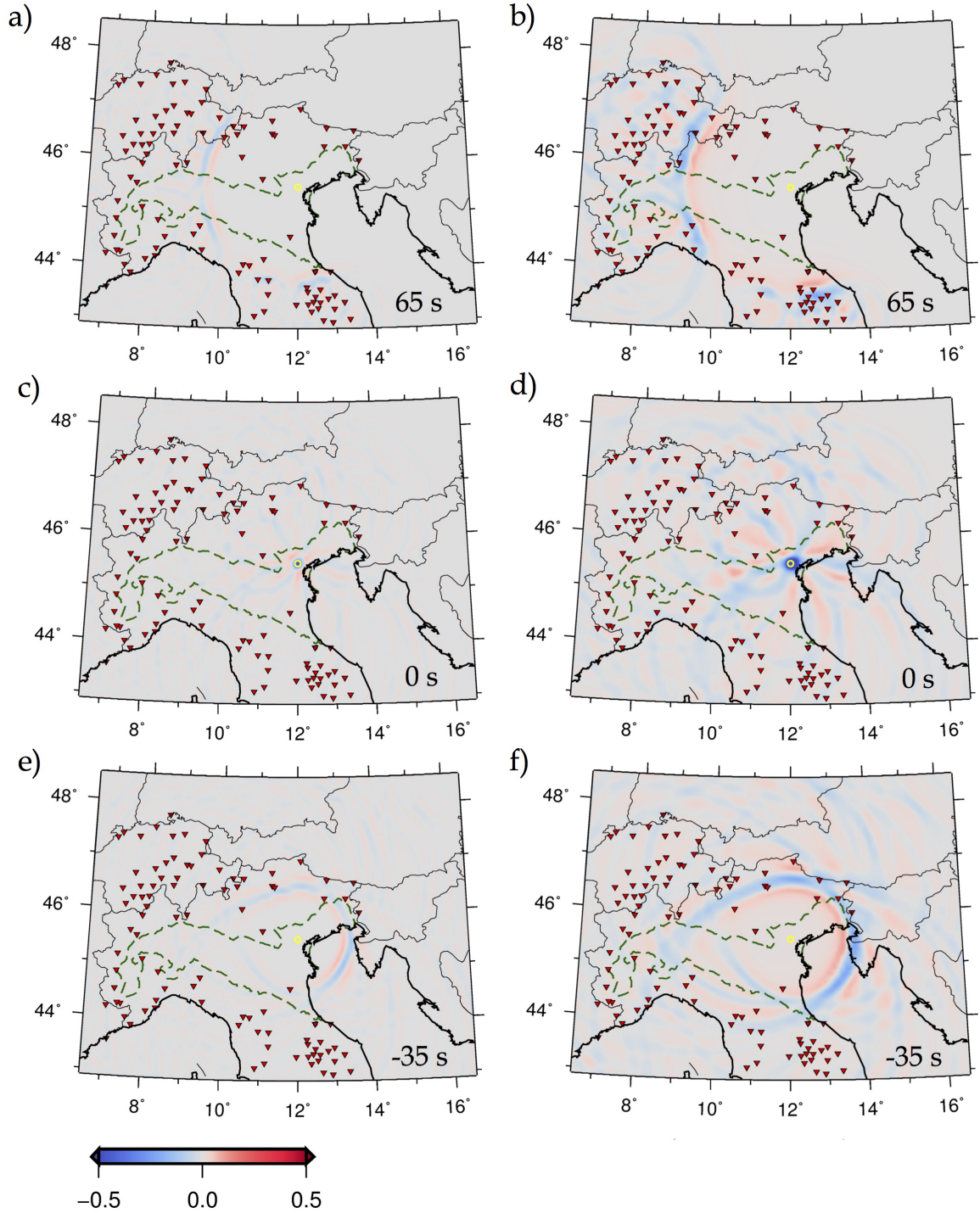


Figure 2: Snapshots of the ray-theory (left) and SPEC-FEM2D (right) synthetic-data time-reversal simulations (sec. 6.1). Station locations are denoted by red triangles, the source location by a yellow circle. We define $t=0$ as the time when the source experiences the maximum displacement according to the Ricker wavelet in the *forward* simulations; backward propagation starts at the time corresponding to the last data sample employed in our exercise, and time increments in time-reversal simulations are considered to be negative. For each of the two time-reversal simulations, amplitudes are normalized to the maximum value obtained in the simulation, corresponding to source location at $t=0$. Snapshots a and b are taken at time $t=65$ s; c and d at $t=0$ s, e and f at $t=-35$ s. As explained in sec. 6, ray-theory and SPEC-FEM2D wave fields can be compared only qualitatively. Snapshots c and d show that the time-reversed wave field focuses at the “epicenter” location.

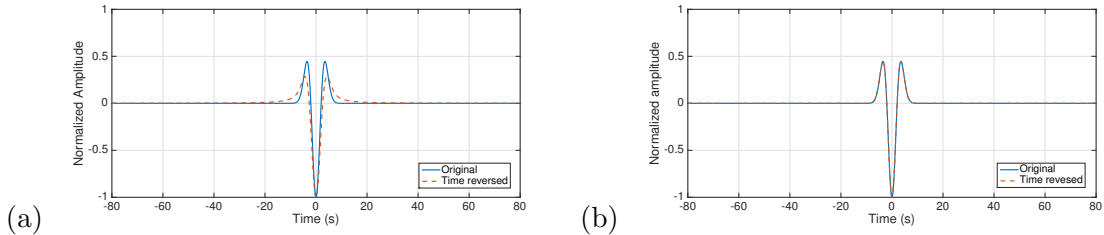


Figure 3: Synthetic test of sec. 6.1: Normalized time-reversed and backward-propagated displacement (dashed red curves) computed at the known location of the source, via (a) SPEC2FEM2D and (b) ray theory. In both cases, the known source time function is shown (blue curve) for comparison. In panel a, the difference between forcing term and reconstructed signal is explained by the fact that, in SPEC2FEM2D, displacement is initiated by prescribing a point force, rather than a displacement as in the ray-theory case.

579 6.2 Ambient-noise cross correlations

580 Cross-correlations of ambient signal form a perfectly suited data set to validate a source-
 581 localization method: each cross-correlation is an approximation for the corresponding receiver-
 582 receiver Green’s function, and the location of both receivers is naturally well known. We select
 583 station LSD.GU (Fig. 5) as our virtual “test” source, and time-reverse and backward propa-
 584 gate ambient-noise based Green’s functions associated with it. (Noise cross correlations will
 585 be described in a separate study [Molinari *et al.*, 2018].) This amounts to implementing
 586 the right-hand side of eq. (39) via our two algorithms. We first Butterworth-filter vertical-
 587 component cross correlations around 16 s (low and high corner frequencies corresponding
 588 to periods of 26 and 6 s, respectively), and, as in sec. 6.1, propagate time-reversed signal
 589 through the Rayleigh-wave phase-velocity map of Fig. 1b. The results of this exercise are
 590 shown in Fig. 4 and Fig. 5. Again, despite the poor azimuthal station coverage in this ex-
 591 ample, the time-reversed wave field focuses quite precisely on the virtual source, in both
 592 the ray-theory and SPEC2FEM2D implementations. In both cases, the maxima of the time-
 593 reversed wave field at the known source location is correctly achieved at $t=0$. Similar to
 594 sec. 6.1, non-physical signal naturally emerges after focusing.

595 If station coverage were uniform and the noise-based Green’s functions perfectly recon-
 596 structed, the time-reversed signal at LSD.GU (Fig. 5) should closely approximate an impulse,
 597 which is not the case. We have seen, however, from the results of sec. 6.1 and in particular
 598 Fig. 3, that the source time function can be reconstructed well even when the station cov-
 599 erage is poor. We infer that artifacts in the trace of Fig. 5 result from inaccuracies in the
 600 reconstructed Green’s function. This is not surprising because, while the phase of Green’s
 601 functions is reconstructed well by ambient-noise cross correlation, their amplitude probably
 602 is not [e.g. Ekström *et al.*, 2009].

603 We next iterate the ray-theory procedure for the 4-to-10 s and 20-to-30 s period bands,
 604 and show the results in Figs. 6 and 7. Membrane-wave propagation is modeled using phase-
 605 velocity maps at 6 and 25 s periods (Fig. 1a, c), respectively, again from Kaestle *et al.* [2017].
 606 The quality of focusing is comparable to the intermediate-period case (Fig. 4), and can be
 607 considered high, in view of the nonuniformity of station distribution. This result confirms
 608 that our algorithm can be applied to a variety of surface-wave modes, and, as far as reliable
 609 phase-velocity and Green’s function estimates are available, is fairly independent of period,

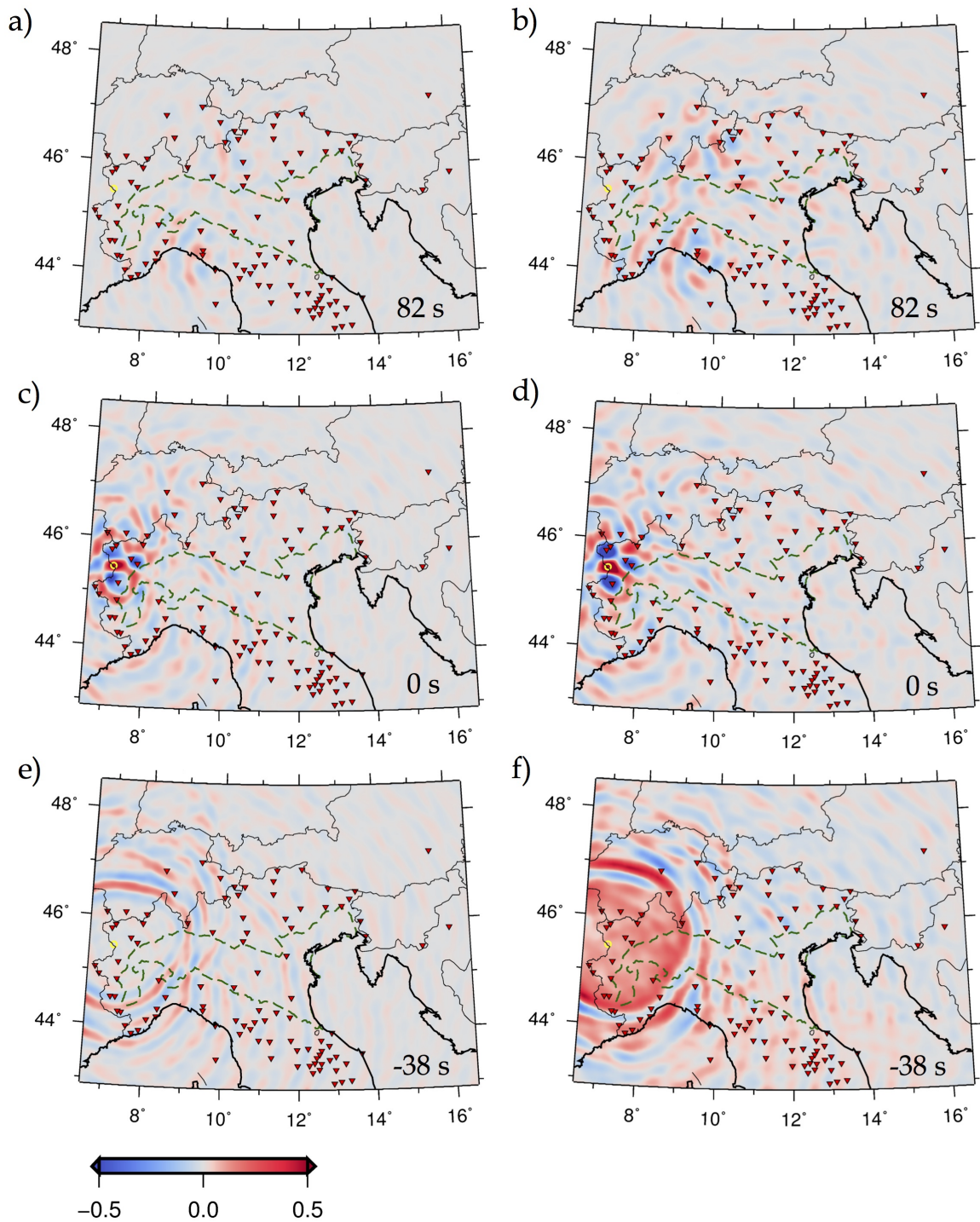


Figure 4: Snapshots of the ray-theory (left) and SPECfEM2D (right) time-reversal simulations of real noise cross-correlations described in sec. 6.2, in the 6-to-26 s period band. This is similar to Fig. 2, but synthetic traces are replaced by cross-correlations of ambient data recorded at station LSD.GU (yellow circle) and all other stations whose locations are denoted by red triangles. Ambient-noise cross-correlations approximate the Green’s function for each station pair, and, in this exercise, station LSD.GU can accordingly be thought of as a “virtual source.” Snapshots a and b are taken at time $t=82$ s; c and d at $t=0$ s, e and f at $t=-38$ s. Snapshots c and d show that the time-reversed wave field indeed focuses at the location of station LSD.GU.

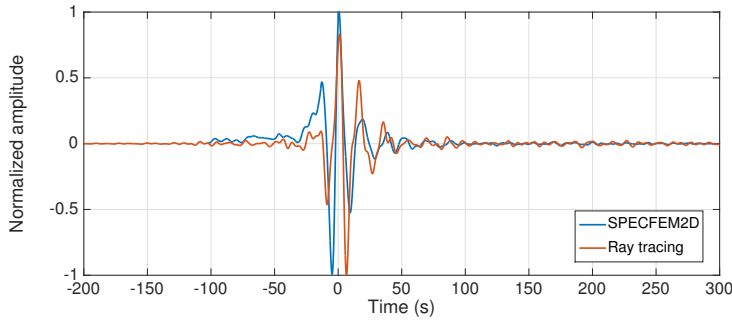


Figure 5: Time-reversed and backward-propagated empirical, ambient-noise based Green’s functions (sec. 6.2), computed at the location of the virtual source, i.e. station LSD.GU, via SPECFEM2D (blue curve) and ray theory (red).

610 and of the width of the passband.

611 6.3 Recordings of the Emilia earthquake of May 29, 2012

612 We apply our ray-theory- and SPECFEM2D-based algorithms to vertical-component record-
613 ings of the magnitude $M_w=5.6$ ($M_I=5.8$) Emilia earthquake of May 29, 2012, 7:00:03 AM.
614 These data, discussed in detail by *Molinari et al.* [2015], are shown here in Fig. 8. Traces are
615 filtered around 16 s, the same way as in sec. 6.2, before time-reversal and backward prop-
616 agation; propagation is modeled according to the 16s Rayleigh-wave phase velocity map of
617 Fig. 1b. Results are summarized in Figs. 9 and 10. Early time-steps (e.g., Fig. 9a,b) are
618 characterized by the emergence of time-reversed late arrivals, that we believe to be associ-
619 ated with reverberations, e.g. at the sharp boundaries between Po plain and surrounding
620 mountain ranges. This signal does not focus sharply anywhere on our membrane, and can
621 accordingly be neglected in this context. Direct-arrival surface waves, on the other hand, do
622 focus at the known epicenter location in both our implementations (Fig. 9c,d). Similar to
623 secs. 6.1 and 6.2, non-physical signal again emerges after focusing (Fig. 9e,f).

624 Fig. 10 shows that the maximum amplitude of the reconstructed vertical displacement
625 at the epicenter occurs at $t=22$ s according to spectral-element time reversal; this delay with
626 respect to the reported earthquake origin time is comparable with the considered surface-wave
627 period, and, in order of magnitude, with typical discrepancies between body- and surface-
628 wave-based estimates of rupture times. The ray-theory simulation results in multiple maxima
629 between 0 and 50 s. All this presumably reflects the complexity of surface-wave generation
630 at the source, as well as errors introduced by the mentioned, non-physical propagation of the
631 time-reversed wave field after focusing.

632 We repeat ray-theory time reversal in the 4-to-10 s and 20-to-30 s passbands, and show
633 the results in Figs. 11 and 12. Focusing of the time-reversed wave field is less sharp both
634 in space and time (although, interestingly, in late snapshots of the time-reversal simulation
635 (Fig. 11e,f), wavefronts are nicely centered on the earthquake epicenter). We ascribe the loss
636 in source localization accuracy to the significant reduction in the width of the passbands,
637 with respect to the previously discussed, 6-to-26 s simulation: we had anticipated in sec. 1
638 that focusing of the time-reversed wave field is enhanced by combining as many time-reversed
639 surface-wave modes as possible. In our future work, we plan to more rigorously take advantage
640 of this effect, multiplication surface-wave potential and their horizontal gradients by the radial

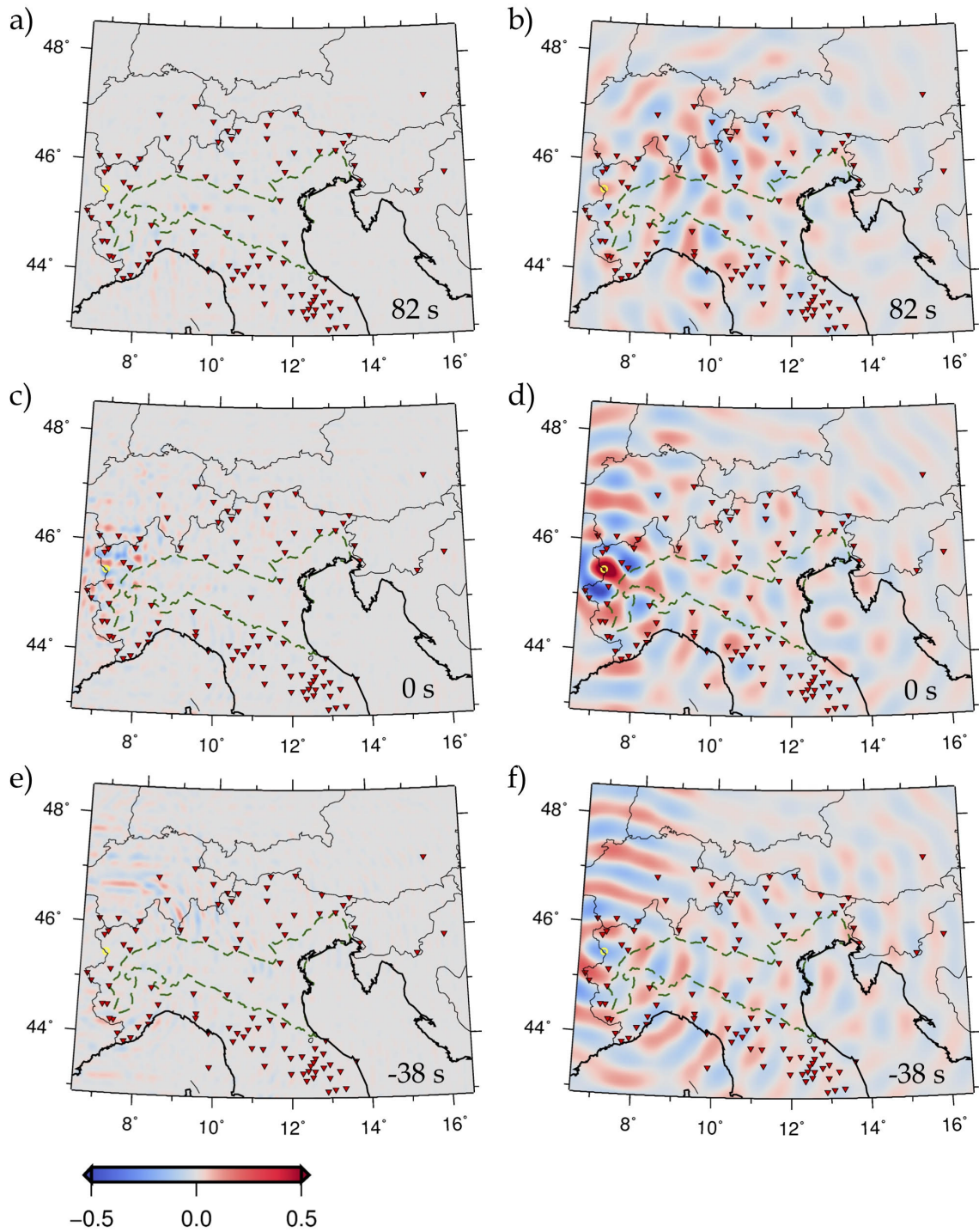


Figure 6: Snapshots of time-reversal simulations of real noise cross-correlations, in the 4-to-10 s (left) and 20-to-30 s (right) period bands. As in Fig. 4, cross-correlated data were recorded at station LSD.GU (yellow circle) and all other stations whose locations are denoted by red triangles. Snapshots were selected at the same times as in Fig. 4. Snapshots c and d show that, also in these period bands, the time-reversed wave field focuses at the location of station LSD.GU.

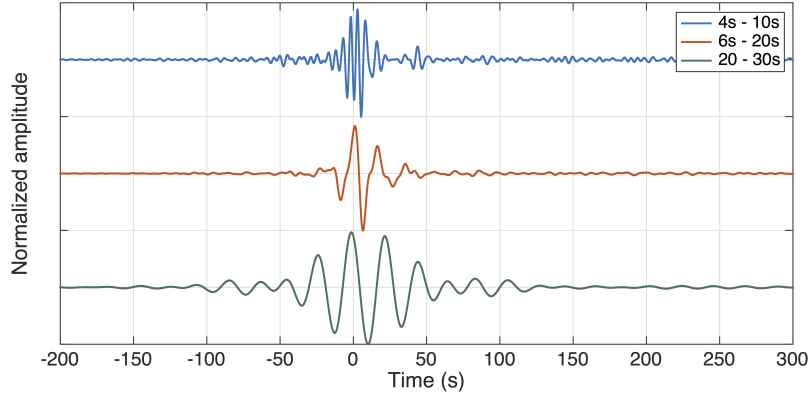


Figure 7: Same as Fig. 5, but traces obtained (via ray theory only) in the period bands 4-to-10 s (blue curve), 6-to-26 s (red) and 10-to-20 s (green) are shown.

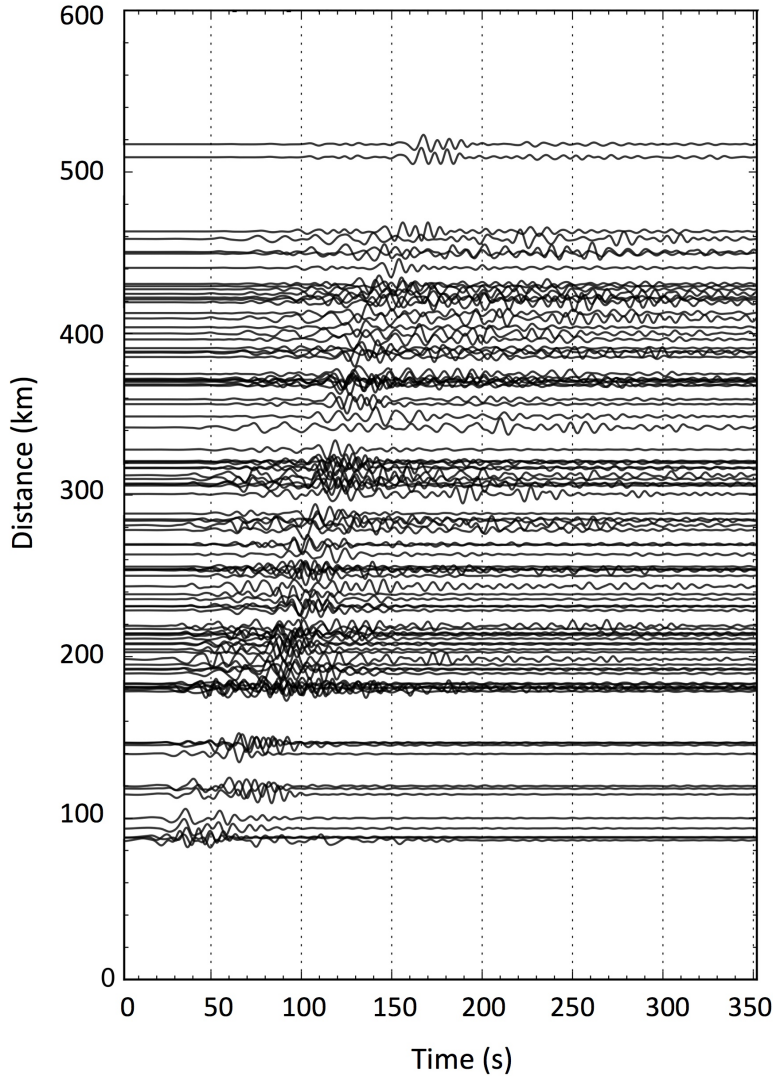


Figure 8: Normalized vertical-component recordings of the Mw=5.6 (MI=5.8) Emilia earthquake of May 29, 2012 [e.g. *Molinari et al.*, 2015], that we time-reverse and backward-propagate as discussed in sec. 6.3. The vertical axis corresponds to epicentral distance, and each trace is plotted about its associated epicentral distance. All traces are Butterworth-filtered around 16 s as described in sec. 6.3.

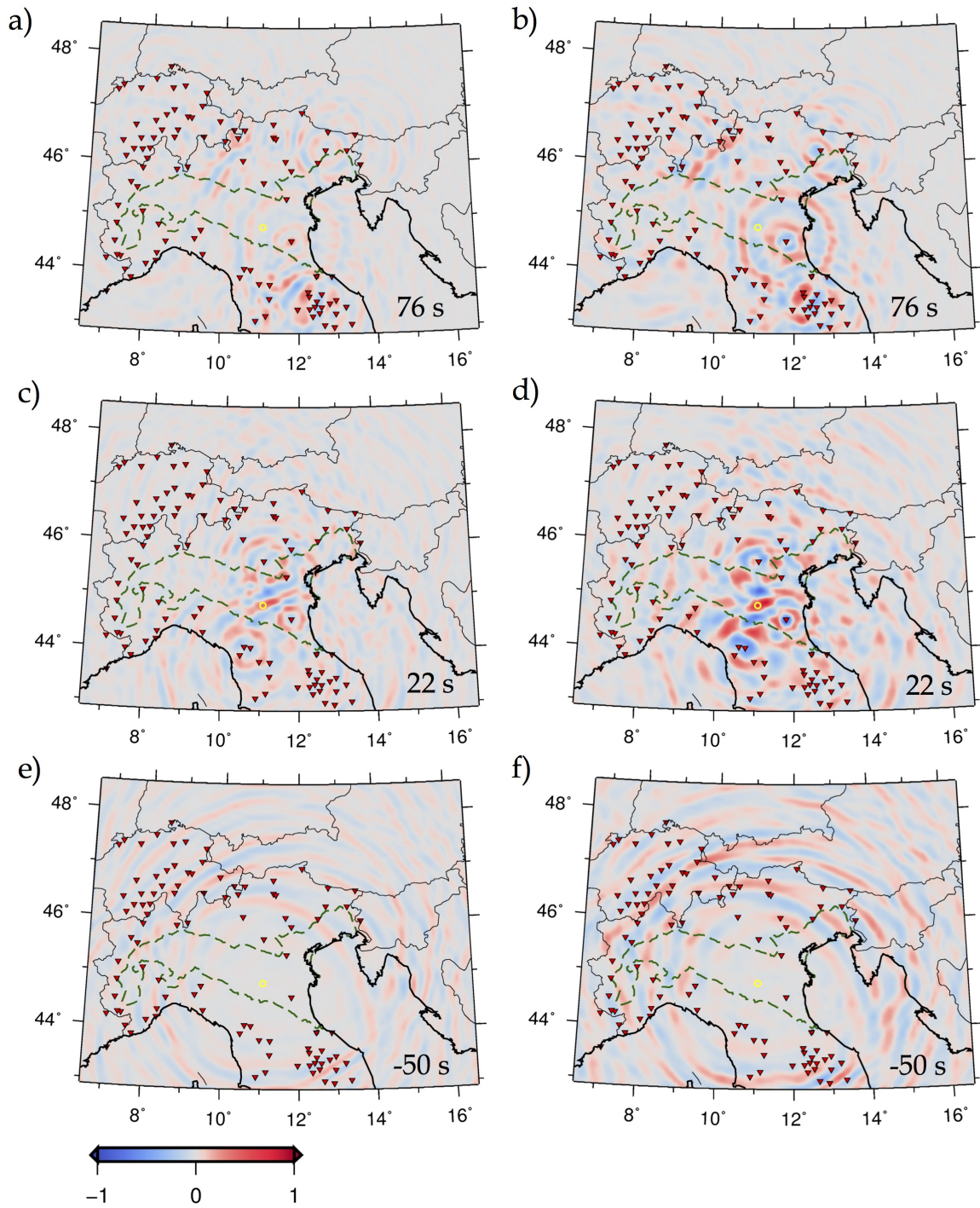


Figure 9: Snapshots of the ray-theory (left) and SPECfEM2D (right) time-reversal simulations of real earthquake data described in sec. 6.3. Again, the locations of stations utilized in the time-reversal simulation are denoted by red triangles, while the earthquake epicenter is marked by a yellow circle. We define $t=0$ as the earthquake origin time as reported by the *Centro Nazionale Terremoti* at INGV. Snapshots a and b are taken at time $t=76$ s; c and d at $t=22$ s, e and f at $t=-50$. Snapshots c and d show that the time-reversed wave field focuses at the epicenter of the earthquake.

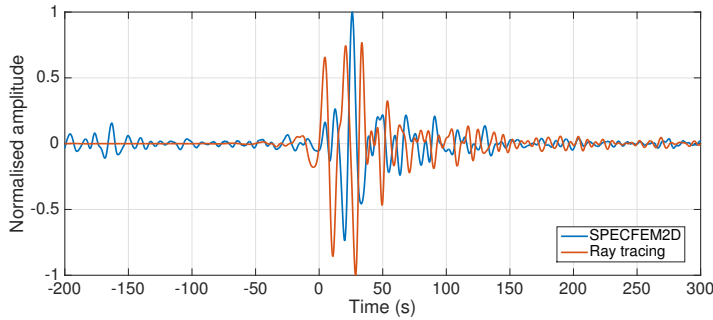


Figure 10: Time-reversed signal at the epicenter of the Emilia earthquake as reconstructed by SPECFEM2D (blue curve) and ray theory (red) time reversal. Again, we define $t=0$ as the earthquake origin time; t should be interpreted as in Fig. 9, i.e. negative t corresponds to time *after* focusing in a time-reversal simulation.

641 eigenfunctions $U(\omega)$, $V(\omega)$, $W(\omega)$ according to eqs. (5) and (6), before integrating over the
 642 entire surface-wave frequency range.

643 Importantly, our analysis of time-reversed earthquake data shows that even at relatively
 644 short epicentral distances, where they are obscured by the body-wave coda, surface waves
 645 can still emerge in a time-reversal exercise. Focusing of the backward-propagated signal at
 646 the source can be thought of as a form of constructive interference. For time-reversed waves
 647 emitted at various station locations to interfere constructively, their backward propagation
 648 has to be modeled correctly. In our approach, time-reversed seismograms are filtered around
 649 one surface-wave frequency, and backward-propagated via the known Green’s function (i.e.
 650 phase-velocity map) for that frequency. In other words, only the propagation of time-reversed
 651 signal associated with surface waves at that frequency is modeled correctly, and it is only
 652 this signal that will contribute to “constructive interference” and to focusing of the time-
 653 reversed wave field. Accordingly, circular wave fronts that can be associated with body-wave
 654 signal, and that do not focus at the epicenter (or elsewhere) are visible in Fig. 9a, b. We
 655 infer that surface-wave time reversal can indeed function as a source-imaging method also
 656 at relatively small epicentral distances, independently of how clearly surface waves can be
 657 identified visually on seismograms.

658 7 Conclusions

659 By taking advantage of the theory of surface-wave “potentials,” we have reduced the problem
 660 of surface-wave propagation to two dimensions (“membrane waves”). We have shown that 3-D
 661 wave fields can then be reconstructed from monochromatic 2-D ones, once radial surface-wave
 662 eigenfunctions (sec. 2) are known; in this study, however, we only studied the propagation of
 663 surface-wave potentials in 2-D. We implemented a surface-wave time-reversal algorithm that
 664 can rely on either spectral-element or ray-theory models of wave propagation. In both cases,
 665 the theory is validated by application to real seismometer arrays in Central Europe. First, a
 666 synthetic test is implemented by computing approximately monochromatic membrane-wave
 667 seismograms at all receiver positions, from an arbitrary selected source location in Northern
 668 Italy. In a second experiment, synthetic traces are replaced by approximate Green’s functions,
 669 obtained by cross-correlating the real ambient signal recorded at one station of the array with

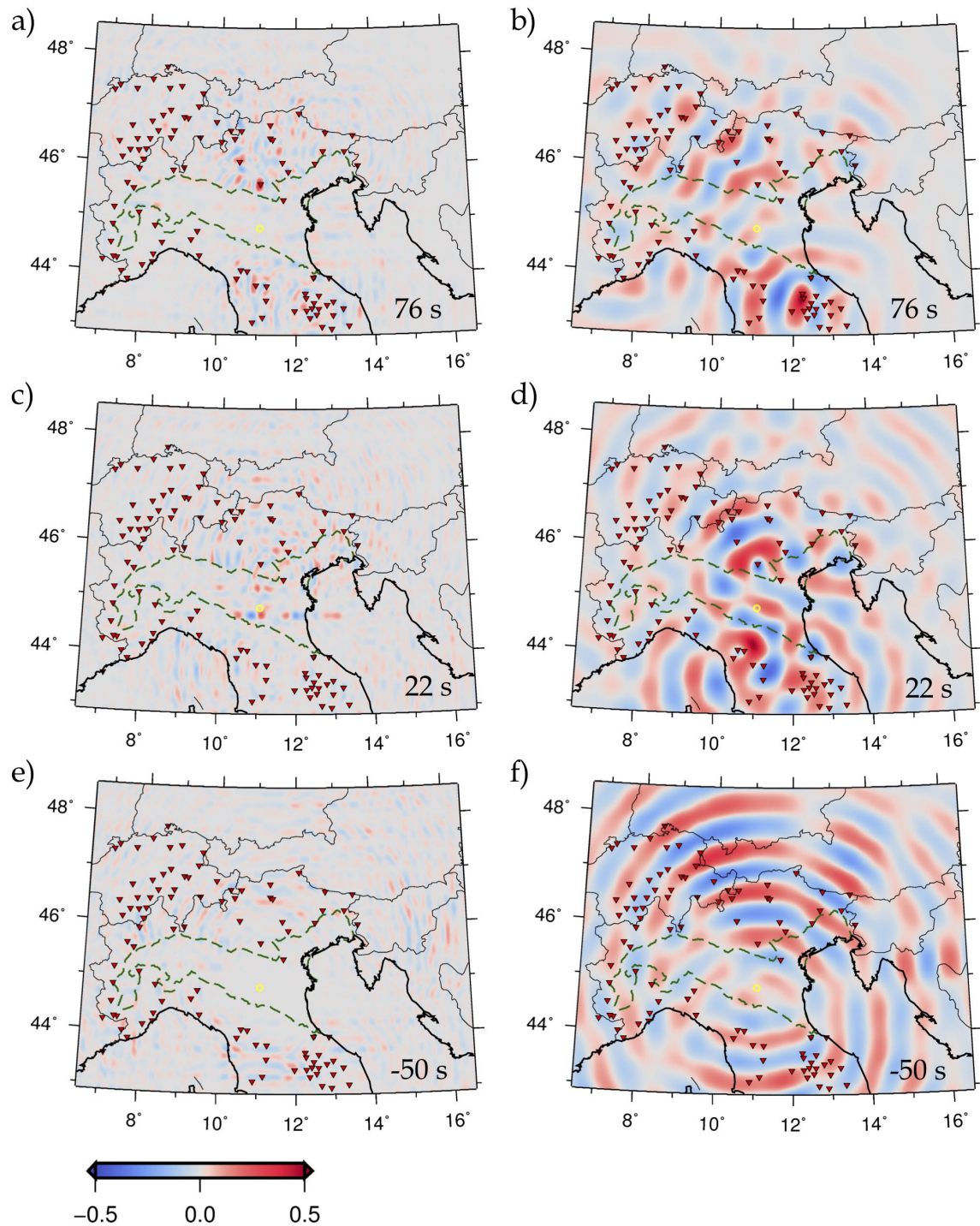


Figure 11: Snapshots of ray-theory time-reversal simulations of real earthquake data, in the 4-to-8 s (left) and 20-to-30 s (right) period bands. Snapshots were selected at the same times as in Fig. 9. All symbols are defined as in Fig. 9.

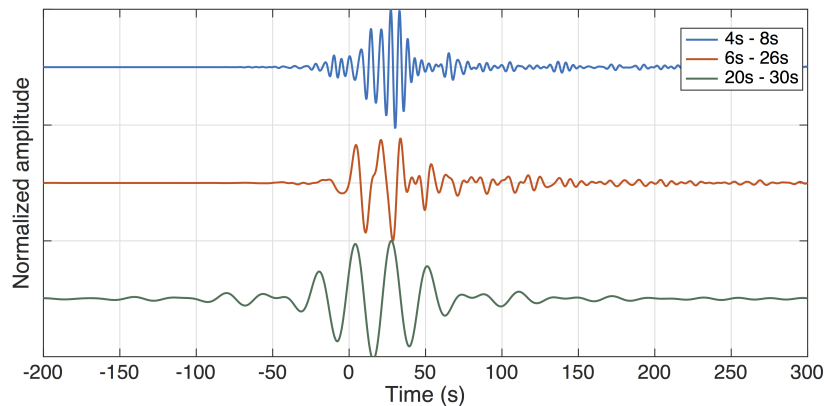


Figure 12: The ray-tracing based trace of Fig. 10 (red curve, 6-to-26s period band) is compared to analogous traces obtained for the 4-to-8s (blue) and 20-to-30s (green) bands. Each trace is normalized to its maximum.

670 that recorded at all other stations. Finally, waveforms from a magnitude-5.6 event in the Po
671 plain are used. In all three cases, time-reversal and backward propagation of the data result in
672 focusing of the signal at the location and time of the source, despite the severe nonuniformity
673 of data coverage, inaccuracies in ambient-noise-based Green’s function reconstruction, and
674 difficulties in disentangling surface-wave signal from the body-wave coda. Importantly, our
675 experiment described in sec. 6.3 suggests that time reversal and backward propagation using
676 the surface-wave Green’s function result in focusing of surface waves at the epicenter even at
677 distances less than teleseismic, where surface waves carry less energy than body waves and
678 their coda. These results encourage further applications of our method, in particular to the
679 task of mapping, in space and time, rupture processes associated with large earthquakes.

680 Acknowledgments

681 We are indebted to Julien de Rosny, Jean-Paul Montagner, Piero Poli, Kees Wapenaar for
682 their insightful advice. Emanuel Kaestle provided his phase-velocity maps while Piero Poli
683 shared his ambient-noise cross correlations. Several figures were created with the Generic
684 Mapping Tools software [Wessel and Smith, 1991], and we made wide use of the ObsPy soft-
685 ware [Krischer et al., 2015]. LB and MR are supported by the European Union’s Horizon
686 2020 research and innovation programme under the Marie Skłodowska-Curie grant agree-
687 ment 641943 (WAVES network). IM is supported by the Swiss National Science Foundation
688 SINERGIA Project CRSII2-154434/1 (Swiss-AlpArray).

689 References

- 690 Aki, K., and P. G. Richards, *Quantitative Seismology, second edition*, University Science
691 Books, Sausalito, CA., 2002.
- 692 Baker, B. B., and E. T. Copson, *The Mathematical Theory of Huygens’ Principle, second*
693 *edition*, Oxford University Press, 1950.
- 694 Boschi, L., and G. Ekström, New images of the Earth’s upper mantle from mea-

- 695 surements of surface wave phase velocity anomalies, *J. Geophys. Res.*, *107*(B4),
696 doi:10.1029/2000JB000,059, 2002.
- 697 Boschi, L., and C. Weemstra, Stationary-phase integrals in the cross-correlation of ambient
698 noise, *Rev. Geophys.*, *53*, doi:10.1002/2014RG000,455, 2015.
- 699 Campillo, M., and P. Roux, Seismic imaging and monitoring with ambient noise correlations,
700 in *Treatise of Geophysics. Vol. 1*, edited by B. Romanowicz and A. M. Dziewonski, Elsevier,
701 2014.
- 702 Derode, A., E. Larose, M. Campillo, and M. Fink, How to estimate the Green’s function of a
703 heterogeneous medium between two passive sensors? Application to acoustic waves, *Appl.*
704 *Phys. Lett.*, *83*(15), 3054–3056, DOI:10.1063/1.1617,373, 2003.
- 705 Ekström, G., A global model of Love and Rayleigh surface wave dispersion and anisotropy,
706 25-250 s, *Geophys. J. Int.*, *187*, 1668–1686, doi:10.1111/j.1365–246X.2011.05,225.x, 2011.
- 707 Ekström, G., G. A. Abers, and S. C. Webb, Determination of surface-wave phase veloci-
708 ties across USArray from noise and Aki’s spectral formulation, *Geophys. Res. Lett.*, *36*,
709 doi:10.1029/2009GL039,131, 2009.
- 710 Fang, H., H. Yao, H. Zhang, Y. C. Huang, and R. D. van der Hilst, Direct inversion of
711 surface wave dispersion for three-dimensional shallow crustal structure based on ray tracing:
712 methodology and application, *Geophys. J. Int.*, *201*, 1251–1263, 2015.
- 713 Fink, M., Time-reversed acoustics, *Scientific American*, *281*, 91–97, 1999.
- 714 Fink, M., Time-reversal acoustics in complex environments, *Geophysics*, *71*(4), SI151–SI164,
715 DOI:10.1190/1.2215,356, 2006.
- 716 Fukahata, Y., Y. Yagi, and L. Rivera, Theoretical relationship between back-projection
717 imaging and classical linear inverse solutions, *Geophys. J. Int.*, *196*, 552–559,
718 doi:10.1093/gji/ggt392, 2014.
- 719 Ide, S., Slip inversion, in *Treatise of Geophysics. Vol. 1*, edited by G. Schubert, pp. 192–223,
720 Elsevier, 2007.
- 721 INGV Seismological Data Centre, Rete Sismica Nazionale (RSN), Istituto Nazionale di Ge-
722 ofisica e Vulcanologia (INGV), Italy, p. doi:10.13127/SD/X0FXnH7QfY, 1997.
- 723 Ishii, M., P. M. Shearer, H. Houston, and J. E. Vidale, Extent, duration and speed of the
724 2004 Sumatra-Andaman earthquake imaged by the Hi-Net array, *Nature*, *435*, 933–936,
725 doi:10.1038/nature03,675, 2005.
- 726 Istituto Nazionale di Oceanografia e di Geofisica Sperimentale, North-East Italy Seismic
727 Network, International Federation of Digital Seismograph Networks, p. doi:10.7914/SN/NI,
728 2002.
- 729 Kaestle, E. D., R. Soomro, C. Weemstra, L. Boschi, and T. Meier, Two-receiver measurements
730 of phase velocity: Cross-validation of ambient-noise and earthquake-based observations,
731 *Geophys. J. Int.*, *207*, 1493–1512, doi:10.1093/gji/ggw341, 2016.

- 732 Kaestle, E. D., A. El-Sharkawy, L. Boschi, T. Meier, C. L. Rosenberg, L. Cristiano, and
733 C. Weidle, Surface-wave tomography of the alps using ambient-noise and earthquake phase-
734 velocity measurements, *J. Geophys. Res.*, *submitted*, 2017.
- 735 Kinsler, L. E., A. R. Frey, A. B. Coppens, and J. V. Sanders, *Fundamentals of Acoustics*
736 (*fourth edition*), Wiley & Sons, Hoboken, N. J., 1999.
- 737 Komatitsch, D., and J. Tromp, Introduction to the spectral element method for three-
738 dimensional seismic wave propagation, *Geophys. J. Int.*, *139*(3), 806–822, 1999.
- 739 Krischer, L., T. Megies, R. Barsch, M. Beyreuther, T. Lecocq, C. Caudron, and J. Wasser-
740 mann, ObsPy: a bridge for seismology into the scientific Python ecosystem, *Computational*
741 *Science and Discovery*, *8*, 014,003, doi:10.1088/1749-4699/8/1/014,003, 2015.
- 742 Larmat, C., J. P. Montagner, M. Fink, E. Clévéde, and A. Tourin, Time-reversal imaging of
743 seismic sources-application to the Sumatra earthquake, *Geophys. Res. Lett.*, *33*, L19,312,
744 doi:10.1029/2006GL026,336, 2006.
- 745 Larmat, C., J. Tromp, Q. Liu, and J. P. Montagner, Time-reversal location of glacial earth-
746 quakes, *J. Geophys. Res.*, *113*, B09,314, doi:10.1029/2008JB005,607, 2008.
- 747 Longuet-Higgins, M. S., A theory of the origin of microseisms, *Phil. Trans. R. Soc. Lond.*,
748 *243*, 1–35, 1950.
- 749 Mai, M., et al., The earthquake-source inversion validation (SIV) project, *Seism. Res. Lett.*,
750 *87*, 690–708, 2016.
- 751 MedNet project partner institutions, Mediterranean Very Broadband Seismographic Net-
752 work (MedNet), Istituto Nazionale di Geofisica e Vulcanologia (INGV), Italy, p.
753 doi:10.13127/SD/fBBtDtd6q, 1988.
- 754 Miller, D. A. B., Huygens’s wave propagation principle corrected, *Optics Letters*, *16*, 1370–
755 1372, 1991.
- 756 Molinari, I., A. Argnani, A. Morelli, and P. Basini, Development and Testing of a 3D Seismic
757 Velocity Model of the Po Plain Sedimentary Basin, Italy, *Bull. Seism. Soc. Am.*, *105*,
758 753764, 2015.
- 759 Molinari, I., P. Poli, A. Morelli, L. Boschi, and R. Cardi, Imaging 3D crustal structure in the
760 presence of deep sedimentary basins: Po-Plain (Italy) case study, *in preparation for Terra*
761 *Nova*, 2018.
- 762 Peter, D., C. Tape, L. Boschi, and J. H. Woodhouse, Surface wave tomography: global
763 membrane waves and adjoint methods, *Geophys. J. Int.*, *171*, 1098–1117, 2007.
- 764 Peter, D., L. Boschi, and J. H. Woodhouse, Tomographic resolution of ray and finite-frequency
765 methods: a membrane-wave investigation, *Geophys. J. Int.*, *177*(2), 624–638, 2009.
- 766 Roten, D., H. Miyake, and K. Koketsu, A Rayleigh wave back-projection method
767 applied to the 2011 Tohoku earthquake, *Geophys. Res. Lett.*, *39*, L02,302,
768 doi:10.1029/2011GL050,183, 2012.

- 769 Snieder, R., Extracting the Green’s function of attenuating heterogeneous acoustic media
770 from uncorrelated waves, *J. Acoust. Soc. Am.*, *121*, 2637–2643, doi:10.1121/1.2713,673,
771 2007.
- 772 Stehly, L., M. Campillo, and N. M. Shapiro, A study of the seismic noise from its long-range
773 correlation properties, *J. Geophys. Res.*, *111*(B10), 2006.
- 774 Swiss Seismological Service (SED) at ETH Zurich, National Seismic Networks of Switzerland,
775 p. doi:10.12686/sed/networks/ch, 1983.
- 776 Takeuchi, H., and M. Saito, Seismic surface waves, *Meth. Comp. Phys.*, *11*, 217–295, 1972.
- 777 Tanimoto, T., Modelling curved surface wave paths: membrane surface wave synthetics,
778 *Geophys. J. Int.*, *102*, 89–100, 1990.
- 779 Tape, C., Q. Liu, and J. Tromp, Finite-frequency tomography using adjoint methods. Method-
780 ology and examples using membrane surface waves, *Geophys. J. Int.*, *168*(3), 1105–1129,
781 2007.
- 782 Tromp, J., and F. Dahlen, Variational principles for surface wave propagation on a laterally
783 heterogeneous Earth–III. Potential representation, *Geophys. J. Int.*, *112*, 195–209, 1993.
- 784 Udías, A., *Principles of Seismology*, Cambridge University Press, Cambridge, U.K., 1999.
- 785 Wapenaar, C. P. A., and A. J. Berkhout, *Elastic Wave Field Extrapolation–Redatuming of*
786 *Single and Multi-Component Seismic Data*, Elsevier, 1989.
- 787 Wapenaar, K., and J. Fokkema, Green’s function representations for seismic interferometry,
788 *Geophysics*, *71*, SI33–SI46, doi:10.1190/1.2213,955, 2006.
- 789 Wessel, P., and W. H. F. Smith, Free software helps map and display data, *EOS Trans. Am.*
790 *Geophys. Union*, *72*, 445–446, 1991.

791 **Appendix: dipole sources**

792 The term “dipole source” refers here to the superposition of two impulsive point sources
793 *of opposite sign*, located at two different points separated by a *very small* distance d . In
794 this study, the concept of dipole emerges from the physical interpretation (sec. 4.2) of equa-
795 tion (34), relating the time-reversed, backward propagating wave field to the signals initially
796 recorded by a receiver array. In the general context of wave physics, dipole sources are used,
797 e.g., to formulate a modern, “corrected” version of Huygens’ principle [*Baker and Copson*,
798 1950; *Miller*, 1991].

799 The mathematical expression for a dipole source can be obtained by first writing the
800 forcing term q defined in sec. 3 as the sum of two equal source distributions $f(\mathbf{x}, \omega)$ shifted
801 in space by the vector \mathbf{d} (of magnitude d) and switched in sign one with respect to the other,
802 i.e.

$$q(\mathbf{x}, \omega) = f(\mathbf{x} + \mathbf{d}) - f(\mathbf{x}). \quad (46)$$

803 A first-order Taylor expansion around the point \mathbf{x}_S then gives

$$f(\mathbf{x} + \mathbf{d}) \approx f(\mathbf{x}) + \mathbf{d} \cdot \nabla_1 f(\mathbf{x}, \mathbf{x}_S). \quad (47)$$

804 Substituting expression (47) into (46), we find

$$q(\mathbf{x}, \omega) \approx \mathbf{d} \cdot \nabla_1 f(\mathbf{x}, \mathbf{x}_S). \quad (48)$$

805 Finally, the sought expression is found by replacing f with a Dirac $\delta(\mathbf{x} - \mathbf{x}_S)$; since q accord-
806 ingly becomes infinitely large at \mathbf{x}_S and zero elsewhere, the magnitude of \mathbf{d} ceases to have
807 meaning and \mathbf{d} can be replaced by the corresponding unit vector $\hat{\mathbf{d}}$, so that

$$q(\mathbf{x}, \omega) = \hat{\mathbf{d}} \cdot \nabla_1 \delta(\mathbf{x} - \mathbf{x}_S) \quad (49)$$

808 [e.g., *Wapenaar and Berkhout*, 1989, sec. I.3.1].

809 Let us next find a simple expression for the response of a medium to dipole forcing. Recall
810 that we have introduced the Green's function $\mathcal{G}_{2D}(\mathbf{x}, \mathbf{x}_S, \omega)$ in sec. 3 as the solution of eq.
811 (23) with $q(\mathbf{x}, \omega) = \delta(\mathbf{x} - \mathbf{x}_S)$, i.e.

$$\nabla_1^2 \mathcal{G}_{2D}(\mathbf{x}, \mathbf{x}_S, \omega) + \frac{\omega^2}{c^2} \mathcal{G}_{2D}(\mathbf{x}, \mathbf{x}_S, \omega) = -i\omega \delta(\mathbf{x} - \mathbf{x}_S). \quad (50)$$

812 Applying the operator $\hat{\mathbf{d}} \cdot \nabla_1$ to both sides of eq. (50) yields

$$\nabla_1^2 \left[\hat{\mathbf{d}} \cdot \nabla_1 \mathcal{G}_{2D}(\mathbf{x}, \mathbf{x}_S, \omega) \right] + \frac{\omega^2}{c^2} \hat{\mathbf{d}} \cdot \nabla_1 \mathcal{G}_{2D}(\mathbf{x}, \mathbf{x}_S, \omega) = -i\omega \hat{\mathbf{d}} \cdot \nabla_1 \delta(\mathbf{x} - \mathbf{x}_S). \quad (51)$$

813 We infer from eq. (51) that the solution of (23) with $q(\mathbf{x}, \omega) = \hat{\mathbf{d}} \cdot \nabla_1 \delta(\mathbf{x} - \mathbf{x}_S)$ is simply
814 $\hat{\mathbf{d}} \cdot \nabla_1 \mathcal{G}_{2D}(\mathbf{x}, \mathbf{x}_S, \omega)$.

815 Alternatively, *Boschi and Weemstra* [2015] (eqs. (E1)-(E3)) define the Green's function
816 G_{2D} in the time domain as the solution of

$$\nabla^2 G_{2D} - \frac{1}{c^2} \frac{\partial^2 G_{2D}}{\partial t^2} = 0 \quad (52)$$

817 with initial conditions

$$G_{2D}(\mathbf{x}, \mathbf{x}_S, 0) = 0, \quad (53)$$

818

$$\frac{\partial G_{2D}}{\partial t}(\mathbf{x}, \mathbf{x}_S, 0) = \delta(\mathbf{x} - \mathbf{x}_S). \quad (54)$$

819 Applying, again, $\hat{\mathbf{d}} \cdot \nabla_1$ to both sides of eqs. (52)-(54), we find that $\hat{\mathbf{d}} \cdot \nabla_1 G_{2D}(\mathbf{x}, \mathbf{x}_S, t)$ is
820 the field resulting from a *dipole initial velocity* at \mathbf{x}_S . This, or rather its Fourier transform
821 $\hat{\mathbf{d}} \cdot \nabla_1 G_{2D}(\mathbf{x}, \mathbf{x}_S, \omega)$, is what we call “dipole response” throughout this study.